# A One-Dimensional Model for Investigating Scale-Separated Approaches to the Interaction of Oceanic Internal Waves

KURT L. POLZIN[a] AND YURI V. LVOV[b]

[a] Woods Hole Oceanographic Institution, Woods Hole, Massachusetts
[b] Department of Mathematical Sciences, Rensselaer Polytechnic Institute, Troy, New York

(Manuscript received 8 September 2023, in final form 3 September 2024, accepted 30 September 2024)

ABSTRACT: High-frequency wave propagation in near-inertial wave shear has, for four decades, been considered fundamental in setting the spectral character of the oceanic internal wave continuum and for transporting energy to wave breaking. We compare idealized ray-tracing numerical results with metrics derived using a wave turbulence derivation for the kinetic equation and a path integral to study this specific process. Statistical metrics include the time-dependent ensemble mean vertical wavenumber, referred to as a mean drift; dispersion about the mean drift; time-lagged correlation estimates of wavenumber; and phase locking of the wave packets with the background. The path integral permits us to identify the mean drift as a resonant process and dispersion about that mean drift as nonresonant. At small inertial wave amplitudes, ray tracing, wave turbulence, and the path integral provide consistent descriptions for the mean drift of wave packets in the spectral domain and dispersion about the mean drift. Extrapolating these results to the background internal wavefield overpredicts downscale energy transports by an order of magnitude. At oceanic amplitudes, however, the numerics support diminished transport and dispersion that coincide with the mean drift time scale becoming similar to the lagged correlation time scale. We parse this as the transition to a non-Markovian process. Despite this decrease, numerical estimates of downscale energy transfer are still too large. We argue that residual differences result from an unwarranted discard of Bragg scattering resonances. Our results support replacing the long-standing interpretive paradigm of extreme scale-separated interactions with a more nuanced slate of "local" interactions in the kinetic equation.

KEYWORDS: Internal waves; Mixing; Nonlinear dynamics

## 1. Introduction

Internal waves are an important piece of the climate system. In the stratified interior, away from the direct influence of the ocean surface boundary layer, they provide the agency by which mass and buoyancy are mixed across density surfaces (MacKinnon et al. 2017). Internal waves are a key piece of mixing at the ocean's bottom boundary, especially over complex topography (Polzin 2004b, 2009). Consequently, there is a significant literature that attempts to link internal waves to mixing, tracking downscale transfers of energy associated with nonlinear interactions through a wave-breaking process to 3D turbulence. This literature concerns three disjoint pieces: observational inference, formal theory encapsulated in a kinetic equation, and knowledge gained from ray-tracing simulations. This work was initiated as an effort to synthesize these three elements, an effort that ultimately ended in failure. This failure has dynamic parallels with 3D turbulence and physics. These three elements are briefly presented below, followed by an extended discussion of the underlying concepts of resonance, scale separation, and spectral transport.

### a. A brief review of internal wave energy cascades

#### 1) OBSERVATIONAL INFERENCE

Gregg (1989) provides us with an assertion that turbulent dissipation $\epsilon \sim \epsilon_0 E^2 N^2$ with $\epsilon_0 \cong 7 \times 10^{-10}$ W kg$^{-1}$, where $E$ is a length scale metric of wave amplitude and buoyancy frequency $N$. Gargett (1990) notes that the bandwidth in Gregg's datasets is insufficient to distinguish $\epsilon \sim N^2$ from alternate scalings such as $\epsilon \sim N^{3/2}$ and that Gregg's metric of $E$ is biased. Wijesekera et al. (1993) provide additional data analysis with CTD data that are consistent with Gregg (1989). Polzin et al. (1995) present datasets with greater bandwidth $N$ and an unbiased metric of $E$ to argue that $\epsilon \sim \epsilon_0 E^2 N^2$ with $\epsilon_0$ agreeing with Gregg (1989) and tertiary variability that plausibly depends upon frequency content or aspect ratio. On a contrary note, Hibiya et al. (2012) present data in which $\epsilon_0$ is 3–4 times smaller. There are likely two issues in play. The first is that the estimates of $\epsilon$ are likely biased low by a factor of 2–3 through the use of the Goodman coherent noise subtraction scheme [T. Ijichi 2023, personal communication; see also Thurnherr et al. (2020)] and a mismatch of the space–time scales in which fine structure and microstructure are being averaged (Whalen 2021). Apart from this amplitude bias issue, Hibiya et al. (2012) also note variability that plausibly depends upon frequency content and provide a metric to assess the enhancement of both near-inertial and continuum wave amplitudes. Polzin et al. (1995) express the frequency content as an aspect ratio using scaling arguments concerning ray-tracing transports in Henyey et al. (1986) and Henyey (1991) to obtain $\epsilon \sim \epsilon_0 E^2 N^2 f$. The estimates of aspect ratio utilize a shear/strain ratio metric available to vertical profiling instrumentation. Such metrics are noted to be biased, i.e., they do not encapsulate the dynamic range that one would obtain if one used a frequency spectrum to estimate the corresponding moment. Gregg et al. (2003) present further data and make a hydrostatic approximation in the algebra for the aspect ratio.

---

Corresponding author: Kurt L. Polzin, kpolzin@whoi.edu

DOI: 10.1175/JPO-D-23-0185.1

© 2025 American Meteorological Society. This published article is licensed under the terms of the default AMS reuse license. For information regarding reuse of this content and general copyright information, consult the AMS Copyright Policy (www.ametsoc.org/PUBSReuseLicenses).

Brought to you by MBL/WHOI Library | Unauthenticated | Downloaded 06/09/25 01:56 PM UTC

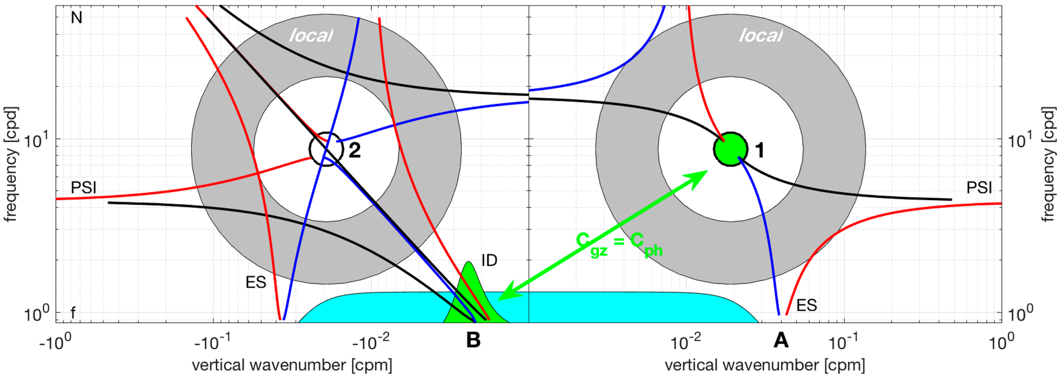

FIG. 1. Solid lines depict the resonant manifold of the internal wave problem [(1)] in the situation where the three horizontal wavevectors are either parallel or antiparallel, plotted in a vertical wavenumber–frequency space, for a wave with ($\mathbf{p}$, $\sigma$) at the center of the green circle. With rotation, extreme scale separations in horizontal wavenumber lead to Bragg scattering (ES) and a phase velocity $C_{\mathrm{ph}}$ equals group velocity $C_g^z$ resonance condition (ID) being located at the Coriolis frequency $f$. This study focuses upon the latter class, with scale separation in both horizontal and vertical wavenumbers. The Bragg scattering resonance is only scale-separated in horizontal wavenumber. Near-resonant ID conditions are depicted in green, and bandwidth-limited nonresonant ID forcing is depicted in cyan. Local interactions are depicted with gray shading. Vertical wavenumber–frequency combinations pertaining to a fourth-order cumulant are labeled 1, 2, A, and B.

This provides a compact expression that is straightforward to evaluate, but one that has even greater bias. Ijichi and Hibiya (2015) provide algebra that corrects for the bias in aspect ratio estimates, essentially codifying in algebra the estimates of bias presented in Fig. A1 of Polzin et al. (1995).

The focus on variable aspect ratio to explain tertiary departures from an $\epsilon \sim \epsilon_0 E^2 N^2 f$ scaling is plausible, but ray-tracing concepts compete with alternative explanations concerning the efficacy of parametric subharmonic instability transports that are a function of power laws and variability in the inertial cusp (Olbers et al. 2020; Dematteis et al. 2024). The endpoint of observational inference is a "finescale parameterization" that is robust but heuristic in nature (Polzin et al. 2014).

### 2) FORMAL THEORY

Wave turbulence (Zakharov et al. 1992; Nazarenko 2011) provides, through an expansion in the strength of interaction that starts with a linear wave basis, a formal basis for assessing the slow time evolution of the wave spectral density associated with weakly nonlinear wave–wave interactions in a small-amplitude limit. This formal approach is built upon the concept of a resonant manifold. For a three-wave system with wavenumbers $\mathbf{p}$, $\mathbf{p}_1$, and $\mathbf{p}_2$ and frequencies $\sigma$, $\sigma_1$, and $\sigma_2$ linked by a dispersion relation, the resonant manifold is defined by solutions to

$$\begin{array}{ll} \sigma = \sigma_1 + \sigma_2 & \mathbf{p} = \mathbf{p}_1 + \mathbf{p}_2 \\ \sigma = \sigma_1 - \sigma_2 & \mathbf{p} = \mathbf{p}_1 - \mathbf{p}_2 \\ \sigma = \sigma_2 - \sigma_1 & \mathbf{p} = \mathbf{p}_2 - \mathbf{p}_1. \end{array} \tag{1}$$

Solutions for $\sigma$ and $\mathbf{p}$ being a high-frequency and high-vertical-wavenumber wave, respectively, are displayed graphically in Fig. 1.

One paradigm happens when one of the three waves has a much greater physical dimension, a scale separation, in at least one spatial coordinate. These limits are referred to as "induced diffusion" (ID), "elastic scattering" (ES), and "parametric subharmonic instability" (PSI) in the oceanographic literature. Physical interpretations for the scale-separated ID and ES interactions are pursued in section 1b(3). Invoking these scale separations allows simplification of the considerable algebraic complexity of the integrand of the kinetic equation.

A second paradigm of "local" interactions happens in the absence of a scale separation. In this paradigm, the kinetic equation refuses to submit to simplification, and one turns to dimensional analysis Polzin (2004a). This differs from Kolmogorov (1941) due to the fact that the resonant manifold lacks a precise three-dimensional symmetry, apparent in Fig. 1, even in the absence of rotation. We refer the reader to Dematteis and Lvov (2021) and Dematteis et al. (2022, 2024) for quantitative characterization of local interactions from the kinetic equation.

Holloway (1980, 1982) provides us with a critique of the internal wave kinetic equation: that, if it could be derived, a kinetic equation that includes finite amplitude resonance broadening will suffer from a Doppler shifting defect in the induced diffusion regime. The theoretical community at that time is using a resonant version, i.e., the infinitesimal amplitude limit of the above, and symptomatic of this are interaction time scales shorter than a wave period, far shorter than the slow time evolution envisioned in the derivation of the kinetic equation. This issue needs to wait for the derivation of that broadened kinetic in Lvov et al. (2012) and further analysis in Polzin and Lvov (2017), in which these short time scales are able to be physically interpreted as an artifact of Doppler shifting.

Ascertaining the practical consequences of this defect, though, requires further effort that this report details.

Brought to you by MBL/WHOI Library | Unauthenticated | Downloaded 06/09/25 01:56 PM UTC

### 3) RAY TRACING

Ray tracing provides an alternate treatment of the induced diffusion regime as it deals directly with Doppler shifting. Early efforts are assessed in a review of internal wave dynamics (Müller et al. 1986). The coauthors of that review appear to accept that the ray-tracing results are phenomenologically different from the induced diffusion limit of the kinetic equation but are unable to make progress. There is speculation that the Doppler shift defect and phenomenological disparities could be encapsulated as an "interaction time" relative to a "decorrelation time" relating to a "Markov approximation" in the context of ray tracing. Yet, again, no progress is made concerning speculation that ray tracing provides a fundamentally different description of the evolution of a statistical ensemble of wave packets or whether the results appear different due to the ray-tracing simulations being run in a strongly nonlinear parameter regime.

There are three major efforts at ray-tracing simulations with the goal of defining downscale transports in the background internal wave spectrum: Henyey et al. (1986), Sun and Kunze (1999b), and Ijichi and Hibiya (2017). After renormalizing results in Henyey et al. (1986) to account for differences in definitions of the background spectrum (see Polzin et al. 1995), ray-tracing-based estimates of dissipation can be construed as remarkably consistent with the observations.

However, there are issues. These assessments share the following:

- Lack of a derivation of ray tracing to articulate the underlying assumptions. This allows Henyey et al. (1986) to state, "ray tracing is not subject to a weak interaction approximation," with the implication that it has fewer restrictions. It is, however, a small-amplitude theory, and this is not appreciated.
- Assessment of downscale transports using an advective closure. This closure is introduced without theoretical support and is inconsistent with statements made in McComas and Bretherton (1977) and Nazarenko et al. (2001).
- The backgrounds in these simulations are not solutions to the nonlinear equations of motion, and thus, the propagation of initial conditions forward in time may not be realistic.
- The simulations have tunable parameters that lead to a plausible order of magnitude ambiguity in downscale transports. These parameters are scale separations between test waves and background and placement of a high-wavenumber cutoff relating to wave breaking to evaluate downscale transports.
- Lack of an analytic solution against which to compare numerical results and with which to understand the potential for numerical artifacts.

In short, the pattern match with the observations is nice, but ray tracing is an asymptotic theory and the pattern match requires accepting the small expansion parameters in the theory to be $O(1)$.

In this work, we introduce a simplified one-dimensional ray-tracing model focused on the interaction of test waves with inertial shear that permits a critical assessment of these issues.

## b. *Decoder ring*

The development of prognostic models for the evolution of nonlinear wave systems is a process that produces a mystifying amount of algebra that emphasizes first principles over physical insight. In the following subsections, we relate some of the basic concepts that assist the reader in arriving at that physical understanding of extreme scale-separated systems.

### 1) POLARIZATION RELATIONS

Assuming a plane wave formulation of $a\,\exp^{i(\mathbf{r}\cdot\mathbf{p}-\sigma t)}$, the linearized $f$-plane equations of motion for 3D velocities ($u$, $v$, and $w$), buoyancy $b = -g\rho/\rho_0$, and pressure perturbation $\pi$ can be manipulated to provide "polarization relations" (Müller and Olbers 1975; Polzin and Lvov 2011):

$$\begin{aligned}
u &= \left(\frac{k_h^2}{m^2|\mathbf{p}|^2}\right)^{1/2} \frac{m^2(k - ifl/\sigma)}{k_h^2}\, a\, e^{i(\mathbf{p}\cdot\mathbf{r}-\sigma t)} \\
v &= \left(\frac{k_h^2}{m^2|\mathbf{p}|^2}\right)^{1/2} \frac{m^2(l + ifk/\sigma)}{k_h^2}\, a\, e^{i(\mathbf{p}\cdot\mathbf{r}-\sigma t)} \\
w &= \left(\frac{k_h^2}{m^2|\mathbf{p}|^2}\right)^{1/2} - ma\, e^{i(\mathbf{p}\cdot\mathbf{r}-\sigma t)} \\
b &= \left(\frac{k_h^2}{m^2|\mathbf{p}|^2}\right)^{1/2} - \frac{imN^2}{\sigma}\, a\, e^{i(\mathbf{p}\cdot\mathbf{r}-\sigma t)} \\
\pi &= \left(\frac{k_h^2}{m^2|\mathbf{p}|^2}\right)^{1/2} - \frac{(N^2 - \sigma^2)}{\sigma}\, a\, e^{i(\mathbf{p}\cdot\mathbf{r}-\sigma t)}.
\end{aligned} \qquad (2)$$

The prefactor in these polarization relations is such that the wave amplitude $a$ is normalized to represent the total energy:

$$E_k + E_v + E_p = aa^*.$$

The total energy is the sum of horizontal kinetic $E_k$, vertical kinetic $E_v$, and potential $E_p$.

### 2) MOMENTUM, ACTION, AND ENERGY

Our interest is in small-amplitude waves propagating in a larger-amplitude, larger *horizontal* scale background, for which we refer the reader to Lvov and Polzin (2024) for an actual derivation. Wave action spectral density

$$n(\mathbf{p}, \mathbf{r}) = a(\mathbf{p}, \mathbf{r})a^*(\mathbf{p}, \mathbf{r})/\omega \qquad (3)$$

is conserved,

$$\frac{\partial n_{\mathbf{p},\mathbf{r}}}{\partial t} + \nabla_{\mathbf{p}}\sigma_{\mathbf{p},\mathbf{r}} \cdot \nabla_{\mathbf{r}} n_{\mathbf{p},\mathbf{r}} - \nabla_{\mathbf{r}}\sigma_{\mathbf{p},\mathbf{r}} \cdot \nabla_{\mathbf{p}} n_{\mathbf{p},\mathbf{r}} = 0,$$

along characteristics (ray trajectories) defined by

$$\begin{aligned}
\dot{\mathbf{r}}(t) &\equiv \nabla_{\mathbf{p}}\sigma_{\mathbf{p},\mathbf{r}} = \overline{\mathbf{U}} + \mathbf{C}_g, \\
\dot{\mathbf{p}}(t) &\equiv -\nabla_{\mathbf{r}}\sigma_{\mathbf{p},\mathbf{r}},
\end{aligned} \qquad (4)$$

Brought to you by MBL/WHOI Library | Unauthenticated | Downloaded 06/09/25 01:56 PM UTC

in which the intrinsic frequency $\omega = \sigma - \mathbf{p}\cdot\mathbf{U}$ plays the role of the Eulerian frequency $\sigma$ in the polarization relations. The latter of these equations are the eikonal representations of geometric optics:

$$\begin{aligned}\dot{k} &= -kU_x - lV_x - mW_x\\ \dot{l} &= -kU_y - lV_y - mW_y\\ \dot{m} &= -kU_z - lV_z - mW_z\,,\end{aligned} \tag{5}$$

where we neglect vertical gradients of background stratification.

The internal wave energy equation is (Müller 1976)

$$\begin{aligned}&\left(\frac{\partial}{\partial t} + U\cdot\nabla_h\right)(E_k + E_p) + \nabla\cdot\overline{\pi'\mathbf{u}'} =\\ &-\overline{u'u'}\,U_x - \overline{u'v'}\,U_y - \overline{v'u'}\,V_x - \overline{v'v'}\,V_y\\ &-\overline{u'w'}\,U_z - N^{-2}\overline{b'u'}\,\overline{b}_x - \overline{v'w'}\,V_z - N^{-2}\overline{b'v'}\,\overline{b}_y.\end{aligned} \tag{6}$$

The polarization relations then provide compact algebraic expressions for the energy exchange, for which we refer the reader to Polzin (2010) and Müller (1976). Our interest here is the vertical coordinate, for which

$$\begin{aligned}\overline{u'w'} - \frac{f}{N^2}\overline{b'v'} &= kC_g^z\frac{aa^*}{\omega}\\ \overline{v'w'} + \frac{f}{N^2}\overline{b'u'} &= lC_g^z\frac{aa^*}{\omega}.\end{aligned} \tag{7}$$

The two terms in the effective stress will cancel each other in the limit that $\omega \to f$ (Ruddick and Joyce 1979): transfers in the vertical coordinate emphasize high-frequency waves. If the background is in thermal wind balance,

$$\begin{aligned}-\overline{u'w'}\,U_z - N^{-2}\overline{b'v'}\,\overline{b}_y &= kC_g^z\frac{aa^*}{\omega}U_z\\ -\overline{v'w'}\,V_z - N^{-2}\overline{b'u'}\,\overline{b}_x &= lC_g^z\frac{aa^*}{\omega}V_z,\end{aligned} \tag{8}$$

and $(k, l)C_g^z aa^*/\omega$ can be parsed as the vertical flux of horizontal angular momentum across an isopycnal surface (Jones 1967; Bretherton 1969) which has a rich history in the zonal-mean literature (Andrews et al. 1987; Polzin 2010) under the phrase Eliassen–Palm flux (Eliassen and Palm 1961). In our work, the background buoyancy perturbations are small, but relation (7) proves invaluable in developing physical insight into the behavior of this nonlinear system.

### 3) THE PLAYERS IN TODAY'S DRAMA

The two players in today's drama are induced diffusion and elastic scattering that represent different limbs of the resonant manifold (Fig. 1) for three wave interactions. Further discussion is presented in section 5c.

#### *(i) Induced diffusion*

Induced diffusion is an example of a generic interaction in which the phase velocity of a large-scale wave is equal to the group velocity of a smaller-scale wave. A schematic of a single background wave and single high-frequency wave packet is rendered in Fig. 2. The high-frequency wave loses energy as its stress $u'w'$ correlates with the background shear $U_z$ [(6)–(8)]. The depicted interaction does not go on forever: the wave packet will change its group velocity as the vertical wavenumber is modulated [(5)] and the wave packet slowly migrates to a different phase of the background.

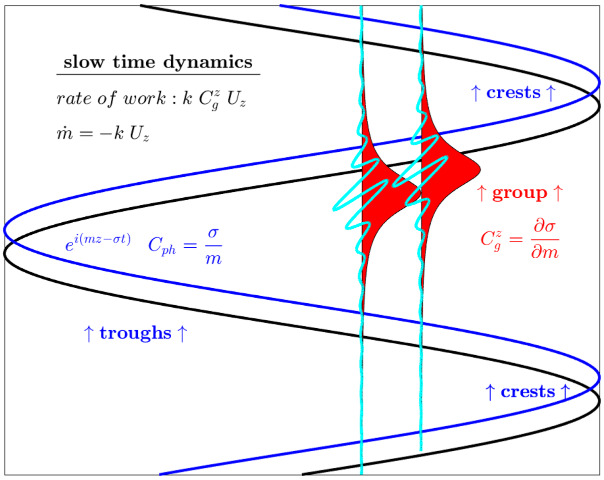

FIG. 2. A schematic of the phase velocity equals group velocity resonance. The large vertical scale sinusoid is depicted with black trace to blue trace implying upward phase propagation. Small vertical scale cyan traces and red envelope structure depict a high-frequency wave packet with upward group velocity going from left to right in the schematic. The wave traces are oriented such that $u'w' > 0$ and the packets are riding within a region of positive vertical shear $U_z$ so that they are losing energy to the large-scale wave at a rate in proportion to $kC_g^z U_z$. The interaction results in a change in the vertical wavenumber $\dot{m}$ of the high-frequency wave so that, as depicted, vertical wavenumber magnitude increases, slowing the wave packet and having it migrate out of the positive shear region on a long time scale.

Assessing this interaction is far more complicated in a random sea of background waves, few of which are resonant at any given time. Questions naturally arise, such as "what are the roles of resonant and nonresonant interactions?" "how do these concepts differ between the kinetic equation and ray tracing?" and "what is the characteristic time that a wave packet will spend in a resonance before decorrelating?" which in turn motivate questions about the average drift of the wave packet in wavenumber and the bandwidth of the resonance. A net energy exchange over all space requires an accumulation of wave packets on the specific phase of the inertial wave relative to the opposing sign of phase. How is this distributed relative to the phase of the near-inertial field at resonance? This structure is obviously different from kinetic theory, which represents the resonant bandwidth as a delta function. An important tool to answer such questions comes about by considering an analogy between a wave packet and a Lagrangian parcel.

The characterization of the phase velocity equals group velocity resonance as a "diffusive" process comes about from a

Brought to you by MBL/WHOI Library | Unauthenticated | Downloaded 06/09/25 01:56 PM UTC

direct analogy to Taylor (1922). We paraphrase. Consider the position of a fluid parcel $x_i$. As a Lagrangian parcel,

$$x_i(t) \equiv \int_{-\infty}^{t} \dot{x}_i(t')dt'. \tag{9}$$

Multiplying both the sides by $\dot{x}_i(t)$, creating an ensemble $\langle \dots \rangle$ over many such particles by summing over $i$ and introducing a change of variables in the difference between time $t$ and $t'$, $\tau = t - t'$:

$$\frac{1}{2}\frac{d\langle x^2 \rangle}{dt} \equiv \int_0^{\infty} \langle \dot{x}(t)\dot{x}(t-\tau)\rangle d\tau. \tag{10}$$

The magic words are "IF this integral converges," the right-hand side will be the product of a velocity variance $\overline{\dot{x}^2}$ and a correlation time scale $\tau_c$:

$$\frac{1}{2}\frac{d\langle x^2 \rangle}{dt} = \langle \dot{x}^2 \rangle \tau_c, \tag{11}$$

so that the second moment $\langle x^2 \rangle$ grows linearly with time:

$$\langle x^2 \rangle \cong 2\langle \dot{x}^2 \rangle \tau_c t = 2Dt, \tag{12}$$

and we refer to $\langle \dot{x}^2 \rangle \tau_c$ as an eddy diffusivity $D$. It is a simple yet very insightful step to substitute wavevector **p** for position vector **r**, motivating a diffusive closure (e.g., McComas and Bretherton 1977; Nazarenko et al. 2001). However, what has not been realized in what is becoming an extensive literature is that, while the IF statement may be true in physical space, it is decidedly unlikely that it will be true in phase space. A first step in trying to fix this will be to introduce a mean drift into (9),

$$x(t) - \langle x(t) \rangle \equiv \int_{-\infty}^{t} \dot{x}(t') - \langle \dot{x}(t') \rangle dt', \tag{13}$$

and hope that the corresponding analysis exhibits a multiple-time-scale behavior. Convergence of the resulting lag correlation analysis on a fast time scale plausibly defines a Markov process in a "weakly" inhomogeneous system.

The seemingly ad hoc introduction of a mean drift actually represents concrete progress. Not only does it provide a definition for an interaction vis correlation time-scale comparison missing from the previous discussions summarized in Müller et al. (1986), in an actual derivation of a packet ensemble action transport equation (Lvov and Polzin 2024), it also provides the missing advective closure utilized in ray-tracing studies.

### *(ii) Elastic scattering*

Elastic scattering is an example of a generic interaction in which the spatial scale of a wave in some dimension is equal to twice that of a larger amplitude "background" which is precisely the character of a Bragg scattering process (Fig. 3). The process figures most prominently in the vertical wavenumber so that the sign of the vertical wavenumber is flipped while the horizontal wavenumber is preserved. With regard to the metric of energy exchange [(8)], flipping the sign of the group velocity provides a reversal in the sign of the energy exchange associated with the phase velocity–group velocity resonance.

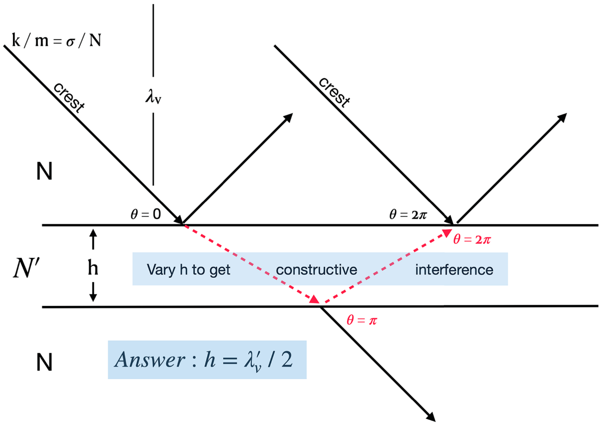

FIG. 3. A schematic of the ES mechanism. A high-frequency wave with downward group velocity partially reflects from an abrupt transition to a higher stratification $N'$. We imagine this high-stratification region has a limited height $h$ so that the wave transmitted from the first "interface" will partially reflect from the second interface. The interface is flat so that the wave is forward scattered in the horizontal. The maximum vertical backscatter is attained when the phases of the waves constructively interfere, which is attained when the height of the middle layer is half the vertical wavelength of the waves in that region, $h = \lambda'_v/2$. This is an example of Bragg scattering. Flipping the sign of the vertical wavenumber flips the sign of the group velocity and thus changes the sign of energy extraction being set up by larger vertical scale background waves with the phase velocity–group velocity resonance in Fig. 2.

This Bragg scattering process does not conserve wave action and implies a damping of the phase velocity–group velocity resonance. This prompts a question of crucial importance: what is the associated damping time scale relative to downscale transports associated with the phase velocity–group velocity resonance?

### 4) TRANSPORT EQUATIONS

We refer the reader to Lvov and Polzin (2024) for side-by-side derivations of Fokker–Planck equations describing the slow time evolution of wave action spectral density $n_{\mathbf{p}}$ from the kinetic equation [(14)] and the evolution of a wave packet ensemble mean action spectral density $\langle n_{\mathbf{p}} \rangle$ [(15)] that starts from the leading-order expression for a single wave packet [(4)].

For the kinetic equation,

$$\frac{\partial n_{\mathbf{p}}}{\partial t} = \frac{\partial}{\partial p_i} D_{ij}(\mathbf{p}, \mathbf{q}) \frac{\partial}{\partial p_j} n_{\mathbf{p}}, \tag{14}$$

with diffusivity tensor

$$D_{ij}(\mathbf{p}, \mathbf{q}) = 8\pi \int d\mathbf{q}(q_i q_j)|V^{\mathbf{p}}_{\mathbf{p}_1,q}|^2 n_q \delta_{\mathbf{p}-\mathbf{p}_1-q} \mathcal{L}(\sigma_{\mathbf{p}} - \sigma_{\mathbf{p}_1} - \sigma_q) d\mathbf{p}_1,$$

where $\mathbf{q} = \mathbf{p} - \mathbf{p}_1$ is a small residual, $V^{\mathbf{p}}_{\mathbf{p}_1,q}$ is the resonant scattering cross sections, and $i$ and $j$ are the Cartesian indices in a 3D spectral domain.

Brought to you by MBL/WHOI Library | Unauthenticated | Downloaded 06/09/25 01:56 PM UTC

For ray tracing,

$$\frac{\partial\langle n_{\mathbf{p}}\rangle}{\partial t} = -\nabla_{\mathbf{p}_i} \cdot \int_{t-\tau}^{t} \mathcal{C}_{ij}(\mathbf{p}, t, t')dt' \cdot \nabla_{\mathbf{p}_j}\langle n_{\mathbf{p}}\rangle - \nabla_{\mathbf{p}_i}\langle \dot{\mathbf{p}}_i\rangle\langle n_{\mathbf{p}}\rangle, \qquad (15)$$

with lagged covariance matrix

$$\mathcal{C}_{ij}(\mathbf{p}, t, t') = \langle\{\dot{\mathbf{p}}[\mathbf{r}(t)] - \langle\dot{\mathbf{p}}[\mathbf{r}(t)]\rangle\}_i\{\dot{\mathbf{p}}[\mathbf{r}(t')] - \langle\dot{\mathbf{p}}[\mathbf{r}(t')]\rangle\}_j\rangle. \qquad (16)$$

Induced diffusion represents the interaction of high-frequency waves with near-inertial shear, and it is the vertical $i = j = 3$ coordinate that dominates the singularities of the integrand in the kinetic equation (Lvov et al. 2010; Dematteis and Lvov 2021). It is the focal point of efforts to understand the spectral character of the internal wave continuum (McComas and Bretherton 1977; McComas and Müller 1981b; Müller et al. 1986). We develop a simple model for this process in this paper. In section 3, we demonstrate that if the time-integrated lagged autocorrelation converges, then

$$D_{33} \to \int_{t-\tau}^{t} \mathcal{C}_{33}(\mathbf{p}, t, t')dt'. \qquad (17)$$

However, predictions for dissipation using the Garrett and Munk model (GM76) spectrum are quite different. The 3D action spectrum $n(\mathbf{p})$ of the GM76 model is independent of vertical wavenumber, $n(\mathbf{p}) \propto m^0$, so that (14) predicts no diffusive transport of action or energy in vertical wavenumber: the predicted dissipation is $\epsilon_0 = 0$. The ray-tracing Fokker–Planck [(15)] contains an advective term representing the ensemble mean drift of wave packets in the spectral domain. We evaluate the associated downscale energy transport in section 5a and find that it predicts an order of magnitude greater dissipation rates than supported by oceanic observations.

To complicate matters, even though expressions for dispersion in vertical wavenumber are similar [(17)], the physical interpretations of the diffusivity tensors are decidedly different. The diffusivity $D_{ij}$ represents a resonant process in kinetic theory, while $C_{ij}$ represents the dispersion about a mean drift $\langle\dot{\mathbf{p}}\rangle$. We demonstrate in section 3 that the mean drift of ray theory is associated with the resonant process and dispersion about the mean drift is driven by nonresonant interactions. The appearance of the mean drift and the nonresonant interpretation of dispersion about that mean drift are contrary to extant derivations of spectral transports in the ray-tracing limit (e.g., McComas and Bretherton 1977; Nazarenko et al. 2001).

This difference in interpretation parallels a fundamental distinction between the kinetic equation and ray tracing. Both begin with expressions for wave amplitude and phase:

$$a(\mathbf{p}, \mathbf{r})e^{i(\mathbf{p}\cdot\mathbf{r}-\sigma t)} \text{ with } n_{\mathbf{p}} = a(\mathbf{p})a^*(\mathbf{p}).$$

The kinetic equation seeks to solve for the slow time evolution of wave amplitude $n_{\mathbf{p}}$ with time-invariant $\mathbf{p}$ and $\sigma$ linked by a dispersion relation. Ray tracing assumes a time-invariant $n(\mathbf{p})$ with a slow time modulation of the constituents of wave phase, $\mathbf{p}$ and $\sigma$, constrained through an intrinsic frequency. These have fundamentally different expressions in terms of bandwidth (Cohen and Lee 1990; Polzin and Lvov 2017) as the former is an amplitude-modulated (AM) process and the latter is a frequency-modulated (FM) process. We note that the AM bandwidth figures prominently in Holloway's complaints.

### c. *An outline for today's efforts*

In this and a companion paper, Lvov and Polzin (2024, hereafter LP), we address and attempt to synthesize the unresolved issues discussed in section 1a. In LP, we provide a derivation which clearly articulates the assumptions underpinning ray tracing and derive Fokker–Planck representations of action transport for induced diffusion in both the kinetic equation and ray tracing. These differ in that the ensemble average wave packet transport equation contains the missing advective closure. The advective closure arises as the diffusivity in induced diffusion is inhomogeneous in the spectral domain. The kinetic equation, as an amplitude-modulated theory for plane waves, represents spectral transports differently from ray tracing, in which wave packets sample this inhomogeneity along their ray trajectories as their vertical wavenumber is modulated.

Knowledge here is gained by creating a stochastic model of high-frequency test waves interacting with a background field of inertial waves (section 2) in which the background is a solution to the nonlinear equations of motion. We present a catalog of diagnostics for the numerical simulations (section 3) that includes the time evolution of spectral moments and lag correlation functions. The stochastic model is designed to provide simple analytic expressions for such diagnostics.

Diagnostics are applied to the ray-tracing output in section 4. Estimates of phase locking (section 4a) between vertical wavenumber and inertial shear clearly document the inertial phase velocity equals high-frequency group velocity coupling that underlies the induced diffusion resonance. The ray-tracing Fokker–Planck introduced in LP permits unambiguous definitions of an interaction time relative to a decorrelation time relating to a Markov approximation. We demonstrate the interplay of the Markov approximation and scale separation in the ray tracing as a finite amplitude effect in section 4b. The first and second moments of the evolving test-wave distributions are compared with the analytic solutions in section 3.

The stochastic model provides an understanding (section 5a) that ray tracing supports downscale energy transports that are an order of magnitude greater than $\epsilon_0$. This understanding is validated in three independent ways: through estimates of the first moment in ray-tracing simulations (section 4b), a path integral assessment of the downscale transport [section 3b(2)], and identification of the mean drift as the gradient of the diffusivity operator from kinetic theory [section 3a(1)].

The result of 10 times too much mixing is at odds with a significant body of observations. We end this contribution (section 5c) by arguing that energy transfers associated with the induced diffusion resonance imply spatially local anisotropic wavefields are short-circuited by a Bragg scattering

Brought to you by MBL/WHOI Library | Unauthenticated | Downloaded 06/09/25 01:56 PM UTC

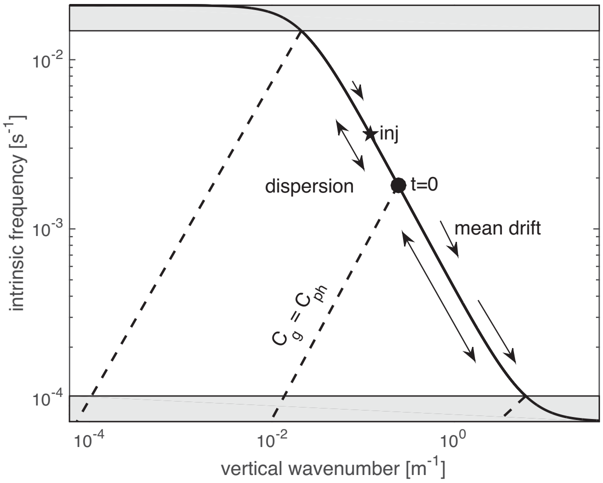

FIG. 4. Schematic of trajectories in a vertical wavenumber–intrinsic frequency space for the one-dimensional model. Test waves are displaced along the solid black line such that $\omega/N = k/m$ with constant $k$. Test waves are released at the black circle. The probability distribution evolves with a mean drift to a higher wavenumber and dispersion about the mean drift. The test waves connect to the inertial field along the lower axis through a phase velocity $f/M$ equals group velocity $(-\omega/m)$ resonance condition (Fig. 2). Note that $m$ and $M$ have opposite signs (Fig. 1). The gray shading denotes the boundary of the model domain where the dispersion relation departs from the hydrostatic, nonrotating limit.

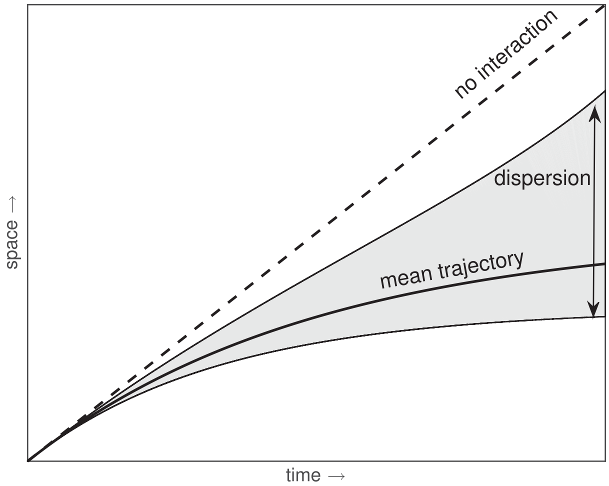

FIG. 5. Schematic of trajectories in space and time for the one-dimensional model. With no interaction, all wave packets follow the dashed line. Interaction with a stochastic inertial shear results in an evolving probability distribution of test-wave vertical wavenumber. We characterize this probability distribution using its first and second moments. Test waves are displaced from the dashed line by interaction with the inertial field. This interaction results in a mean drift toward higher vertical wavenumber and consequently smaller group velocity with dispersion (gray shading) about that mean drift.

resonance acting on the same time scale. We present this as an eddy-damped quasi-normal Markovian closure that parallels the damping of third-order energy transfers by fourth-order cumulants in three-dimensional turbulence. Our results support replacing the long-standing interpretive paradigm of high-frequency action diffusion with a paradigm based upon a more nuanced slate of local resonant interactions (Fig. 1) in the kinetic equation.

We summarize in section 6 and point out that the particle analogy does not end with a path integral and Bragg scattering. The damping also has a parallel originating in solid-state physics, in which a doped conductor makes an abrupt dynamical transition to an insulating state known as "Anderson localization" and points toward the potential for assessing this damping using techniques in open quantum systems.

## 2. A scale-invariant model of wave refraction in inertial shear

### a. *Ray equations*

In this section, we describe a one-dimensional numerical ray-tracing model similar to that presented in Polzin and Lvov (2017). The model uses (18) to represent the evolution of high-frequency test waves having wavenumber $\mathbf{p} = (k, 0, m)$ along trajectories in the vertical wavenumber–intrinsic frequency space as in Fig. 4 and in space–time as in Fig. 5. We refer the reader to LP for a derivation of the eikonal relations $\dot{\mathbf{p}} = -\nabla_{\mathbf{r}}\sigma(\mathbf{p}, \mathbf{r})$ and $\dot{r} = \nabla_{\mathbf{p}}\sigma(\mathbf{p}, \mathbf{r})$ that define ray trajectories in the wavenumber $\mathbf{p} = (\mathbf{k}, m)$ and spatial $\mathbf{r} = (x, y, z)$ domains from an Eulerian frequency $\sigma(\mathbf{p}, \mathbf{r})$ rendered as Eq. (3.18) in LP. The one-dimensional model equations are

$$\begin{aligned} \dot{m} &= -k\partial_z \mathcal{U}(z, t), \\ \dot{z} &= \partial_m \omega, \\ \omega^2 - f^2 &= k^2N^2/m^2, \end{aligned} \tag{18}$$

where $k$ is the horizontal wavenumber, aligned with a purely horizontal background inertial flow $\mathcal{U}(z, t)$; $m$ is the vertical wavenumber; $\omega$ is the intrinsic frequency; $f$ is the Coriolis frequency; and · indicates a time derivative.

### b. *Model formulation*

The backgrounds (19) and (20) comprised a field of randomly phased inertial oscillations having no horizontal structure and a white vertical shear spectrum that extends to oceanographically unrealistic large wavelengths, i.e., a small bandwidth parameter $m_*$. The lack of horizontal structure and vertical velocity implies that the sum of an arbitrary number of such waves is a solution to the nonlinear equations of motion. The specification of an excessively small bandwidth $m_*$ ensures that the results for packet dispersion are scale-invariant and thus leads to simple diagnostics. In this paper, we employ a stratification ($N$) that is 4 times larger than the nominal 3-cph metric used in Polzin and Lvov (2017) in order to move the spectral boundaries away from the initial release site. The large-scale background consists of a random inertial wavefield:

$$\mathcal{U}(z, t) = \sum_i U_i \sin(M_i z - ft + \phi_i), \tag{19}$$

Brought to you by MBL/WHOI Library | Unauthenticated | Downloaded 06/09/25 01:56 PM UTC

TABLE 1. Run summary. We create an ensemble of test-wave time series with a number of test wave (tw) realizations of the randomly phased inertial field having a number of background wave (bw) constituents uniformly distributed in vertical wavenumber between $j_{\min} \times \pi/1300$ m and $j_{\max} \times \pi/1300$ m. The length of the simulations is denoted by the number of time steps at the indicated time difference. The initial condition $m(t = 0)$ is quoted in equivalent mode number $j = m(t = 0)\pi/1300$ m. The length of the simulations (column 3) is that required to get the test-wave distribution to touch the edges of the spectral domain in Fig. 4. The number of test waves (column 4) is dictated by the convergence of lag correlation statistics. The number of background waves (column 5) was selected such that the resonant bandwidth [(45)] would be occupied by multiple randomly phased background waves. The intent is that the resonance is not dominated by a single background wave. The spectral bandwidth parameters $j_{\min}$ and $j_{\max}$ (columns 7 and 8, respectively) are determined by the interest in setting up a scale-invariant system and the geometric constraints of the experimental domain. The last column contains figure number references.

| Name | $e_0/e_0^{\mathrm{GM}}$ | Time step | No. of tw | No. of bw | ss | $j_{\min}$ | $j_{\max}$ | $m(t = 0)$ | Figure No. |
|---|---|---|---|---|---|---|---|---|---|
| run j3 | $10^0$ | 5000@1/10$N$ | 20 000 | 24 001 | 1 | 0.025 | 1600 | $j = 100$ | 7–11 |
| run k3 | $10^0$ | 5000@1/10$N$ | 20 000 | 24 001 | $1/\pi$ | 0.025 | 1600 | $j = 100$ | 9 |
| run l3 | $10^0$ | 5000@1/10$N$ | 20 000 | 24 001 | $\pi$ | 0.025 | 1600 | $j = 100$ | 9 |
| run ll3 | $10^0$ | 5000@1/10$N$ | 20 000 | 24 001 | $2\pi$ | 0.025 | 1600 | $j = 100$ | |
| run m3 | 0.50 | 10 000@1/10$N$ | 20 000 | 24 001 | 1 | 0.025 | 1600 | $j = 100$ | 9 |
| run n3 | 0.50 | 10 000@1/10$N$ | 20 000 | 24 001 | $\pi$ | 0.025 | 1600 | $j = 100$ | 9 |
| run p3 | 0.25 | 20 000@1/10$N$ | 20 000 | 24 001 | 1 | 0.025 | 1600 | $j = 100$ | 9 |
| run q3 | 0.25 | 20 000@1/10$N$ | 20 000 | 24 001 | $\pi$ | 0.025 | 1600 | $j = 100$ | 9 |
| run g3 | $10^{-1}$ | 20 000@1/10$N$ | 10 000 | 24 001 | 1 | 0.025 | 1600 | $j = 100$ | 7–11 |
| run h3 | $10^{-1}$ | 20 000@1/10$N$ | 10 000 | 24 001 | $1/\pi$ | 0.025 | 1600 | $j = 100$ | 9 |
| run i3 | $10^{-1}$ | 20 000@1/10$N$ | 10 000 | 24 001 | $\pi$ | 0.025 | 1600 | $j = 100$ | 9 |
| run a3$_1$ | $10^{-2}$ | 240 000@1/10$N$ | 2000 | 24 001 | 1 | 0.025 | 1600 | $j = 100$ | 7–11 |
| run a3$_2$ | $10^{-2}$ | 240 000@1/10$N$ | 2000 | 24 001 | 1 | 0.025 | 1600 | $j = 100$ | 7–11 |
| run a3$_3$ | $10^{-2}$ | 240 000@1/10$N$ | 2000 | 24 001 | 1 | 0.025 | 1600 | $j = 100$ | 7–11 |
| run a3$_4$ | $10^{-2}$ | 240 000@1/10$N$ | 2000 | 24 001 | 1 | 0.025 | 1600 | $j = 100$ | 7–11 |
| run a3$_5$ | $10^{-2}$ | 240 000@1/10$N$ | 2000 | 24 001 | 1 | 0.025 | 1600 | $j = 100$ | 7–11 |
| run d3$_1$ | $10^{-3}$ | 800 000@1/5$N$ | 1000 | 24 001 | 1 | 0.025 | 1600 | $j = 100$ | 6–11 |
| run d3$_2$ | $10^{-3}$ | 800 000@1/5$N$ | 1000 | 24 001 | 1 | 0.025 | 1600 | $j = 100$ | 7–11 |
| run d3$_3$ | $10^{-3}$ | 800 000@1/5$N$ | 1000 | 24 001 | 1 | 0.025 | 1600 | $j = 100$ | 7–11 |
| run d3$_4$ | $10^{-3}$ | 800 000@1/5$N$ | 1000 | 24 001 | 1 | 0.025 | 1600 | $j = 100$ | 7–11 |
| run d3$_5$ | $10^{-3}$ | 800 000@1/5$N$ | 1000 | 24 001 | 1 | 0.025 | 1600 | $j = 100$ | 7–11 |
| run d3$_6$ | $10^{-3}$ | 800 000@1/5$N$ | 1000 | 24 001 | 1 | 0.025 | 1600 | $j = 100$ | 7–11 |
| run d3$_7$ | $10^{-3}$ | 800 000@1/5$N$ | 1000 | 24 001 | 1 | 0.025 | 1600 | $j = 100$ | 7–11 |
| run d3$_8$ | $10^{-3}$ | 800 000@1/5$N$ | 1000 | 24 001 | 1 | 0.025 | 1600 | $j = 100$ | 7–11 |
| run d3$_9$ | $10^{-3}$ | 800 000@1/5$N$ | 1000 | 24 001 | 1 | 0.025 | 1600 | $j = 100$ | 7–11 |
| run d3$_{10}$ | $10^{-3}$ | 800 000@1/5$N$ | 1000 | 24 001 | 1 | 0.025 | 1600 | $j = 100$ | 7–11 |
| run e3 | $10^{-3}$ | 800 000@1/5$N$ | 1000 | 24 001 | $1/\pi$ | 0.025 | 1600 | $j = 100$ | 6 |
| run f3 | $10^{-3}$ | 800 000@1/5$N$ | 1000 | 24 001 | $\pi$ | 0.025 | 1600 | $j = 100$ | 6 |

with $1/40 \le M_i/j_1 \le 1600$ and the mode one equivalent $j_1 = \pi/1300$ m$^{-1}$. In contrast to Polzin and Lvov (2017), a slightly more sophisticated scale separation between wave and background [(20)] is enforced by a single pole filter:

$$U_i \to U_i \times \sqrt{M_i^2/\{[M_i^2 + (j_1/32)]^2\} * [1 + (\mathrm{ss}M_i/m)^2]}, \qquad (20)$$

with time-dependent $m$ and variable scale selection factor ss. We regard this as nothing more than an ad hoc device to enforce a spatial smoothing on the envelope scale when information on the envelope has long since been discarded (see section 3.2.1 of LP), in order to assess the sensitivity of the mean drift in wavenumber and dispersion of packets about that drift. Run parameters appear in Table 1.

This formulation has been selected with the intent that the vertical wavenumber spectra of vertical shear are independent of vertical wavenumber for $j_1/32 \ll M_i \ll m/\mathrm{ss}$. We use an aphysically small vertical wavenumber bandwidth parameter $j_1/32$ and large stratification (12 cph) to enable us to study the long time evolution with analytic scale-invariant diagnostics presented in section 3. In doing so, the results can be directly related to the GM76 spectrum, in which the level of the vertical wavenumber shear spectrum is proportional to the combination $e_0 m_*$, independent of vertical wavenumber $m$, where $e_0$ is the total energy (nominally 0.0030 m$^2$ s$^{-2}$) and $m_*$ is the vertical wavenumber bandwidth parameter (nominally $4\pi/1300$ m$^{-1}$). The one-sided vertical wavenumber–frequency energy spectrum is

$$e(m, \sigma) = e_0 \frac{2m_*}{\pi}\frac{1}{m_*^2 + m^2}\frac{2f}{\pi}\frac{1}{\sigma(\sigma^2 - f^2)^{1/2}}, \qquad (21)$$

with $n(\mathbf{p}) = e(\mathbf{p})/\sigma_{\mathbf{p}}$. The ray-tracing results will be presented as increments of GM, but what is intended is the dynamically relevant combination $e_0 m_*$. This two-sided vertical wavenumber power spectral density (PSD) of one horizontal component shear has an asymptotic level of

Brought to you by MBL/WHOI Library | Unauthenticated | Downloaded 06/09/25 01:56 PM UTC

$$\mathrm{PSD(GM, two\text{-}sided, one\text{-}component\ shear)} = \frac{3}{4\pi} m_* e_0. \tag{22}$$

At oceanic levels, the one-sided vertical wavenumber power spectrum of two-component shear is approximately $1.0N_0^2\ \mathrm{m}^{-1}$ with $N_0 = 3$ cph.

Test waves are traced in $m$ (Fig. 4) and in $z$ (Fig. 5) as a function of time using a simple forward difference scheme in (18). Values of the random phase $\phi_i$ are stored to permit quantification of the total phase $M_i z - ft + \phi_i$ in (19). Ensemble averages are generated by averaging over tens of thousands of test waves.

Test waves are released at a vertical wavenumber $m$ equivalent to mode 50 ($50\pi/1300\ \mathrm{m}^{-1}$). The analysis starts at a time $t = 0$ when the wave packet crosses the equivalent mode 100, $m_0 \equiv m(t = 0) = 100\pi/1300$. The analysis period ends when a small fraction (<1%) of the wave packets have intrinsic frequencies larger than $N/\sqrt{2}$ or intrinsic frequencies smaller than $\sqrt{2}f$ (Fig. 4). These metrics signify departures of the dispersion relation from its nonrotating hydrostatic approximation and thus the absence of scale-invariant behavior. Despite such conditioning, subtle nonscale-invariant behavior is noted in the latter half of all simulations.

## 3. Metrics of transport

In this study of high-frequency internal wave interactions with near-inertial shear, there are three distinct paradigms. All three are considered to be scale separated in *horizontal* wavenumber, rendering them distinct from *local* interactions graphically depicted in Fig. 1. These three are the phase velocity–group velocity resonance, a Bragg scattering resonance at half the vertical wavelength of the high-frequency wave, and an assortment of nonresonant interactions. The first and last are treated by ray-tracing techniques. Bragg scattering is eliminated from ray tracing at the point of invoking a Wigner transform and Taylor series expansion that is focused upon the phase velocity–group velocity resonance, for which we refer the interested reader to LP. This section seeks to build tools for the analysis of ray-tracing simulations, for which there are subtle but crucial differences between kinetic theory [(14)] and ray tracing [(15)].

### a. *Kinetic equation*

#### 1) FOKKER–PLANCK EQUATION

The moment method is a methodology for the interpretation of a Fokker–Planck equation. For internal waves, this is (14). For our one-dimensional model, (14) reduces to

$$\frac{\partial}{\partial t} n(m, t) + \frac{\partial}{\partial m} D_{33}(m) \frac{\partial}{\partial m} n(m, t) = 0. \tag{23}$$

The vertical–vertical component of the diffusivity tensor $D_{33}$ [Eq. (47); Polzin and Lvov 2017] from the kinetic equation is

$$D_{33} = \pi k^2 f \int d\mathbf{p}_1 n(\mathbf{p}_1) m_1^2 \delta\left(m_1 \frac{\sigma}{m} - \sigma_1\right). \tag{24}$$

The action density $n(\mathbf{p})$ represents the high-frequency field and $n(\mathbf{p}_1)$ represents the inertial background. Our inertial wave model is two-dimensional in the $x$–$z$ plane so that $n(\mathbf{p}_1) = n(k_1, 0, m_1)\delta(l_1)$ in which $n(k_1, m_1) = (1/4)[e(\sigma_1, m_1)/\sigma_1](d\sigma_1/dk_1)$, and the corresponding normalized frequency spectrum is $\delta(\sigma_1 - f)$. The diffusivity is estimated by integrating over horizontal azimuth, changing variables from horizontal wavenumber magnitude to wave frequency, and integrating over vertical wavenumber. The factor $e_0$ represents the total internal wave energy, kinetic plus potential. These are in a ratio of 3:1 for the GM76 model. Our inertial wave model has no potential energy. Incorporating this into (24), we find

$$D_{33}^{1D} = \frac{3}{8} \frac{k m^2 e_0 m_*}{N}. \tag{25}$$

#### 2) MOMENTS

The moment method proceeds by multiplying the diffusion equation by $m^j$, utilizing the chain rule, integrating over the spectral domain, and discarding terms at $m = \pm\infty$ to produce differential equations for the $j$th moment. Here, $\langle \ldots \rangle$ represents the integral over vertical wavenumber.

$$\begin{aligned} \langle n(m) \rangle_t &= 0, \\ \langle m n(m) \rangle_t &= \langle \partial_m (D_{33}) n(m) \rangle, \\ \langle m^2 n(m) \rangle_t &= \langle \partial_m (2m D_{33}) n(m) \rangle. \end{aligned} \tag{26}$$

These moments have analytic solutions for our scale-invariant model:

$$\begin{aligned} \langle m \rangle &= m_0 e^{2D_{33}t/m^2}, \\ \langle m^2 \rangle &= m_0^2 e^{6D_{33}t/m^2}, \\ \langle (m - \langle m \rangle)^2 \rangle &= \langle m^2 \rangle - \langle m \rangle^2. \end{aligned} \tag{27}$$

### b. *Ray path methods*

#### 1) FOKKER–PLANCK EQUATION

In LP, we use ray path techniques to formulate an ensemble average transport [(15)]. In one dimension, this reduces to

$$\frac{\partial \langle n_\mathbf{p} \rangle}{\partial t} = -\nabla_m \cdot \mathcal{C}_{33}(\mathbf{p}) \cdot \nabla_m \langle n_\mathbf{p} \rangle - \nabla_m \langle \dot{m} \rangle \langle n_\mathbf{p} \rangle, \tag{28}$$

with time-integrated lagged autocorrelation function

$$\mathcal{C}_{33}(\mathbf{p}) = \int_{t-\tau}^{t} dt' \langle [\dot{m}[\mathbf{r}(t)] - \langle \dot{m}[\mathbf{r}(t)] \rangle][\dot{m}[\mathbf{r}(t')] - \langle \dot{m}[\mathbf{r}(t')] \rangle] \rangle. \tag{29}$$

Note that both the first and second moments of the ensemble average action density appear explicitly in the transport equation.

Brought to you by MBL/WHOI Library | Unauthenticated | Downloaded 06/09/25 01:56 PM UTC

### 2) A PATH INTEGRAL FOR THE MEAN DRIFT

Here, we present a derivation for the mean drift $\langle \dot{m} \rangle$. We start at (18) and represent the background shear with its inverse Fourier transform:

$$\dot{m} = -k\mathcal{U}_z = -\frac{k}{2\pi}\int_{-\infty}^{\infty} \Upsilon_z(M)e^{i(Mz-ft)}dM. \tag{30}$$

The factor $\Upsilon_z$ represents the Fourier coefficient for vertical shear [(22)]. The vertical coordinate following the ray path is the time integral of the vertical group velocity $C_g^z$. For internal waves,

$$z(t) = \int_{-\infty}^{t} \frac{-kN}{m(t')^2}dt'.$$

The major contributions to the integral [(30)] come from conditions in which the inertial phase velocity $f/M$ is equal to the internal wave group velocity, $C_g^z = -\text{sgn}(m)(|k|N/m^2)$. In the ray coordinate, $z$ is a function of time, and integration in time permits the application of a stationary phase approximation to solve (30). There is a phase

$$\vartheta(t) = -M\int_{-\infty}^{t} dt' \frac{kN}{m^2} - ft, \tag{31}$$

differentiating with respect to time,

$$\dot{\vartheta} = -M\frac{kN}{m^2} - f, \tag{32}$$

and differentiating once more,

$$\ddot{\vartheta} = M\frac{2kN}{m^3}\dot{m}. \tag{33}$$

After Taylor series expanding the phase about the resonance $M_r = -fm^2/kN$, the wave phase in (30) becomes

$$e^{i(Mz-ft)} \to e^{i\{\vartheta(t_0)+[\ddot{\vartheta}(t_0)(t-t_0)^2/2]+\ldots\}}.$$

Changing the variable of integration from $M$ to $t$ by considering the background wavenumber $M$ to be a property of the time-evolving resonance along the ray path returns

$$\int dM \to \int dM_r|_{t=t_0} + \int \frac{dM_r}{dt}\bigg|_{t=t_0} dt\ldots,$$

and applying the stationary phase formula (Bender and Orszag 1978), we obtain

$$1 \cong -k\sqrt{\frac{\pi m^3}{kN\dot{m}}}\frac{2mf}{kN}\left[\frac{1}{2\pi}\frac{\|\Upsilon_z(M_r)\|}{\sqrt{M_r}}\right]\cos\left[\pm\frac{\pi}{4} + \vartheta(t_0)\right], \tag{34}$$

with a choice of sign depending upon the value of $\ddot{\vartheta}(t_0)$. We square both sides of (34) to obtain

$$\dot{m} = -4\pi m^3 \frac{f}{N^2}\left[\frac{1}{2\pi}\|\Upsilon_z(M_r)\|\right]^2 \cos^2\left[\pm\frac{\pi}{4} + \vartheta(t_0)\right], \tag{35}$$

and average over a vertical wavelength

$$\overline{\dot{m}}^z = \frac{1}{\lambda_v}\int_{-\lambda_v/2}^{+\lambda_v/2} \dot{m}\,dz = \frac{1}{\lambda_v}\int_{-\pi}^{+\pi} \dot{m}\frac{dz}{d\vartheta}d\vartheta.$$

We then construct an ensemble average $\langle \overline{\dot{m}}^z \rangle$ by uniformly weighting all possible initial conditions $\vartheta(t_0)$:

$$\left\langle \int_{-\pi}^{+\pi} \cos^2\left[\pm\frac{\pi}{4} + \vartheta(t_0)\right]d\vartheta \right\rangle = \pi.$$

This ensemble represents a sum over all possible paths encoded in the phase function $\vartheta$, and thus, the ensemble average represents a "path integral." Upon recognizing the definition of the PSD given the choice of $\lambda_v$ for a transform interval,

$$\frac{2\pi}{\lambda_v}\left[\left(\frac{1}{2\pi}\right)^2 \Upsilon_z(M_r)\Upsilon_z^*(M_r)\right] \equiv \text{PSD},$$

we obtain, for the GM model in which PSD = $(3/4\pi)m_*e_0$,

$$\langle \overline{\dot{m}}^z \rangle = \frac{3}{4}\frac{kmm_*e_0}{N}. \tag{36}$$

The mean drift is equivalent to $\partial_m D_{33}^{1D}$ derived from kinetic theory [(25)]. Note that the mean drift is arrived at as a resonant process.

### 3) LAG CORRELATION FUNCTIONS AND SECOND MOMENTS

The lagged autocorrelation function

$$\frac{1}{2}\frac{d(m-\langle m \rangle)^2}{dt} = k^2\int_{t-\tau}^{t} [\mathcal{U}_z(t) - \langle \mathcal{U}_z(t) \rangle][\mathcal{U}_z(t-\tau) - \langle \mathcal{U}_z(t-\tau) \rangle]d\tau \tag{37}$$

is the one-dimensional representation for $\mathcal{C}_{33}$ [(29)]. A prediction for the lag correlation function and thus variance can be obtained by noting that the high-wavenumber inertial shear is stationary in the time required for a high-frequency wave packet to propagate through that shear. This suggests replacing the Doppler shift of Taylor's "frozen field" hypothesis with an encounter frequency $s$ representing the time rate of change along a ray:

$$s = MC_g^z, \tag{38}$$

where $C_g^z$ is the vertical group velocity. We investigate by assuming ergotic statistics at small amplitude and invoking the Wiener–Khinchin theorem. Thus,

$$\frac{1}{2}\frac{d(m-\langle m \rangle)^2}{dt} = k^2\int_{t-\tau}^{t}\int_{0}^{+\infty} \cos(s\tau)P_{\mathcal{U}_z}(s)ds\,d\tau, \tag{39}$$

in which $s$ is the encounter frequency along the ray and $P_{\mathcal{U}_z}(s) = P_{\mathcal{U}_z}(M)dM/ds$ is the shear spectral density in that coordinate. From a purely empirical standpoint, the spectra of vertical shear

Brought to you by MBL/WHOI Library | Unauthenticated | Downloaded 06/09/25 01:56 PM UTC

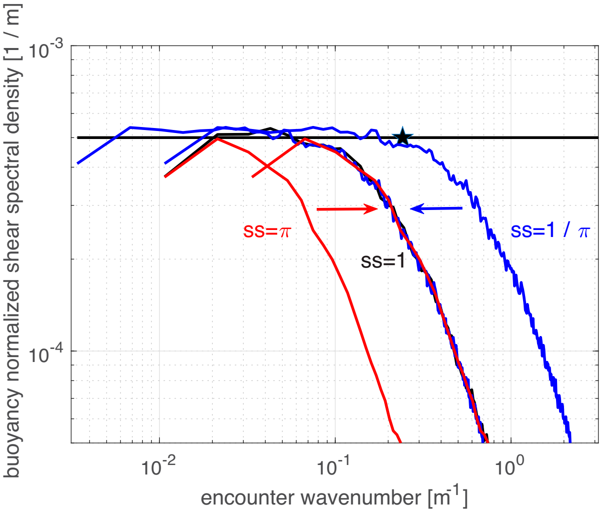

FIG. 6. Example of a frequency spectrum of vertical shear following a ray path for backgrounds with GM × $10^{-3}$, converted to an encounter wavenumber using the group velocity. Results for scale separation factors $\mathrm{ss} = [\pi, 1, \pi^{-1}]$ are indicated using red, black, and blue traces. The spectra are collapsed after rescaling the frequency by ss (indicated by arrows), and the black trace is buried. Such spectra are bandwidth-limited and white with a 1/2 power point at $m(t = 0)$ for $\mathrm{ss} = 1$ denoted by the pentagram. The black horizontal line represents one side of the GM vertical wavenumber shear spectrum, $0.001 e_0 m_* N^{-2} = 0.5 \times 10^{-3}$ m. This spectral description is essentially consistent with using the time domain Fourier transform partner [(20), (40)] of an exponential autocorrelation function [(41)].

in encounter frequency $s$ (Fig. 6) are bandwidth-limited and white. Much of the variability collapses onto

$$P_{\mathcal{U}_z}(s) = \frac{3}{4\pi}\frac{e_0 m_*/C_g^z}{1+\left(\mathrm{ss}\dfrac{s}{\langle\omega\rangle}\right)^2}, \tag{40}$$

which can be derived from the spectrum [(21)] using the change of variables [(38)] and filter [(20)]. Carrying out the cosine transform, we obtain

$$\frac{1}{2}\frac{d(m-\langle m\rangle)^2}{dt} \cong k^2\frac{3}{8}\frac{e_0 m_*}{C_g^z}\frac{\langle\omega\rangle}{\mathrm{ss}}\int_{t-\tau}^{t} e^{-\langle\omega\rangle t/\mathrm{ss}}\,d\tau. \tag{41}$$

If $\langle\omega\rangle$ is regarded as a constant,

$$\frac{1}{2}\frac{d(m-\langle m\rangle)^2}{dt} \cong \frac{3}{4}\frac{km^2 e_0 m_*}{N}\left[1-e^{-\langle\omega\rangle t/\mathrm{ss}}\right]. \tag{42}$$

This prompts several interpretations. The first is the identification of a diffusivity. In the limit that $\langle m\rangle/\langle\dot{m}\rangle \gg \mathrm{ss}/\langle\omega\rangle \equiv \tau_c$, the diffusivity is just

$$D_{33} \cong k^2\langle\mathcal{U}_z^2\rangle\tau_c \text{ with } \tau_c = \frac{\mathrm{ss}}{\langle\omega\rangle} \quad \text{and}$$

$$\langle\mathcal{U}_z^2\rangle = \frac{3}{4\pi}e_0 m_*\int_0^\infty \frac{dM}{1+\left(\mathrm{ss}\dfrac{M_i}{m}\right)^2} = \frac{3}{8}\frac{m}{\mathrm{ss}}e_0 m_*,$$

which is equivalent to that arrived at from resonant theory [(25)]. Note that $\tau_c$ is controlled by the scale separation criterion ss. However, since the encounter spectrum of vertical shear is white, it really does not matter what the scale selection factor ss is; the product $\langle\mathcal{U}_z^2\rangle\tau_c$ is a constant for a white spectrum, as long as the integral [(41)] has converged. Conversely, if the background vertical shear spectrum was other than uniform in vertical wavenumber, variations in the scale separation ss would have a weak influence on the diffusivity.

The second interpretation is that the long time limit in (41), in which effects of the mean drift on the ensemble average frequency $\langle\omega\rangle$ are neglected, is identifiable as the Markov approximation. Our numerical results for moments and lag correlation in section 4b suggest that this approximation is challenged at oceanic amplitudes.

The third interpretation is that the diffusivity results from a nonresonant process: the bandwidth of the integrand in (41) is not the resonant bandwidth from the ray numerics in Figs. 7 and 8 or from kinetic theory. This result is in direct contrast to McComas and Bretherton (1977) and Nazarenko et al. (2001), who present derivations that reduce the diffusivity to a delta function representation of the resonant manifold, represented as the solid lines in Fig. 1. Those derivations implicitly assume the background is statistically homogeneous in the spectral domain and omit an explicit reference to an ensemble averaging process and associated time-dependent ensemble average drift $\langle\dot{m}\rangle$ in (37). They then utilize a Taylor series expansion about a *time-invariant resonance* after representing the vertical wavenumber tendency $\dot{m}$ in terms of its inverse Fourier transform [(30)].

## 4. Numerical results

Our diagnostics include numerical evaluations of probability distributions of inertial wave phase sampled by the high-frequency waves, moments of test-wave vertical wavenumber, and lag correlation analyses in test-wave vertical wavenumber. The probability distributions demonstrate phase locking about the resonant phase velocity equals group velocity condition even at oceanic amplitudes. The moment analysis quantifies an inhibition of the second moment at oceanic amplitudes. The first moment, upon which the ray-tracing closure [(28)] hinges, is less sensitive, but departures are still noted. The lag correlation analysis quantifies the departure of the second moment from its resonant prediction as being a competition between the mean drift and the correlation time scale imposed by an ad hoc scale separation criterion [(20)].

### a. *Phase locking*

#### 1) PHASE PROBABILITY DISTRIBUTIONS

Kinetic equations assume a zeroth-order description in which wave phases are uncorrelated and then predict action transfer associated with phase locking at first order. The inference of phase locking is indirect as one is closing out a hierarchy of moments.

In ray tracing, phase locking can be much more directly assessed (Fig. 7). In this one-dimensional system, the probability

Brought to you by MBL/WHOI Library | Unauthenticated | Downloaded 06/09/25 01:56 PM UTC

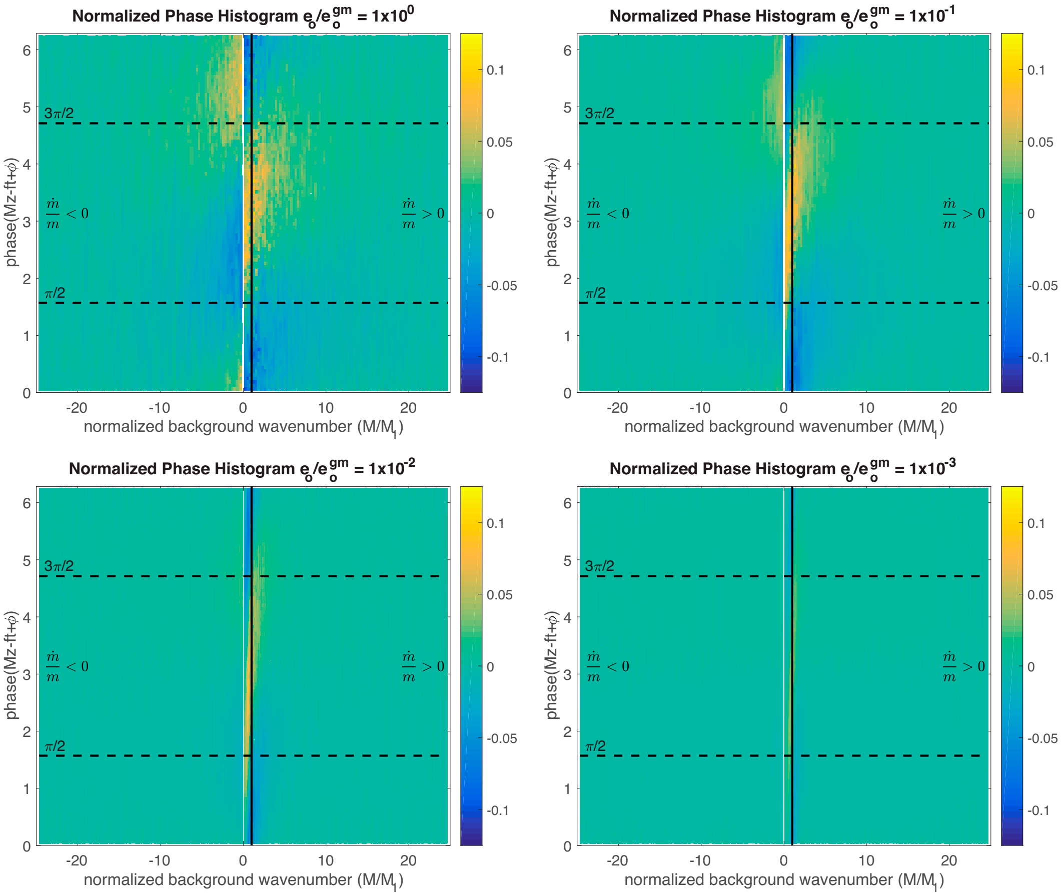

FIG. 7. Deviations of the phase $\vartheta_i = M_i z - ft + \phi_i$ from a uniform distribution as a function of background wavenumber $M_i$ normalized by resonance condition $f/C_g$. The histograms are normalized such that a value of 0.1 indicates a 10% increase in the probability density. The vertical black lines denote the approximate resonance condition $C_{ph} = C_g^z$. Upper-left, upper-right, lower-left, and lower-right panels are $10^0$GM, $10^{-1}$GM, $10^{-2}$GM, and $10^{-3}$GM, respectively.

density $\hat p$ of background phase $\vartheta_i$ [(19)] is estimated as a function of background wavenumber $M_i$:

$$\vartheta_i = M_i z - ft + \phi_i.$$

When the test wave has the value $m_0 - \delta \le m \le m_0 + \delta$,

$$\hat p = p[(\vartheta, M)|m = m_0 \pm \delta],$$

with $m_0$ being equal to the equivalent of mode 100. Since the background shear $\mathcal{U}_z$ is specified as a sum of cosines in (19), a probability density maximum centered about either $\vartheta = \pi/2$ or $\vartheta = 3\pi/2$ implies a bound wave behavior in which the test wave preferentially occupies a background crest or trough and oscillates about the crest/trough. Probability extrema centered on $\vartheta = 0$ or $\vartheta = \pi$ weight [(19)] to return a nonzero average shear and drift to either larger or small scales. In all our runs, the probability extrema occur in association with the resonance $MC_g^z = f$, and maxima are located about $\pi/2 < \vartheta < 3\pi/2$, indicating a net drift of test waves to smaller scales (Fig. 7). The shoulders of the resonance appear more representative of a bound wave behavior.

### 2) BANDWIDTH AND MEAN SHEAR

A quantitative measure of the downscale transport ensemble average $\langle \dot m\rangle = -k\langle \mathcal{U}_z\rangle$ can be obtained from the phase distributions in Fig. 7. The ensemble-averaged shear is

$$\langle \mathcal{U}_z\rangle \propto \int_{-\infty}^{+\infty} dM \int_0^{2\pi} \hat p(\vartheta, M)\cos(\vartheta)d\vartheta, \tag{43}$$

so that the phase average,

$$\int_0^{2\pi} \hat p(\vartheta, M)\cos(\vartheta)d\vartheta, \tag{44}$$

provides a metric of the amplitude and bandwidth of the energy transfer process. These phase-averaged distributions (Fig. 8) are neither peaked precisely at the nominal resonance nor are the distributions symmetric about the peak. However,

Brought to you by MBL/WHOI Library | Unauthenticated | Downloaded 06/09/25 01:56 PM UTC

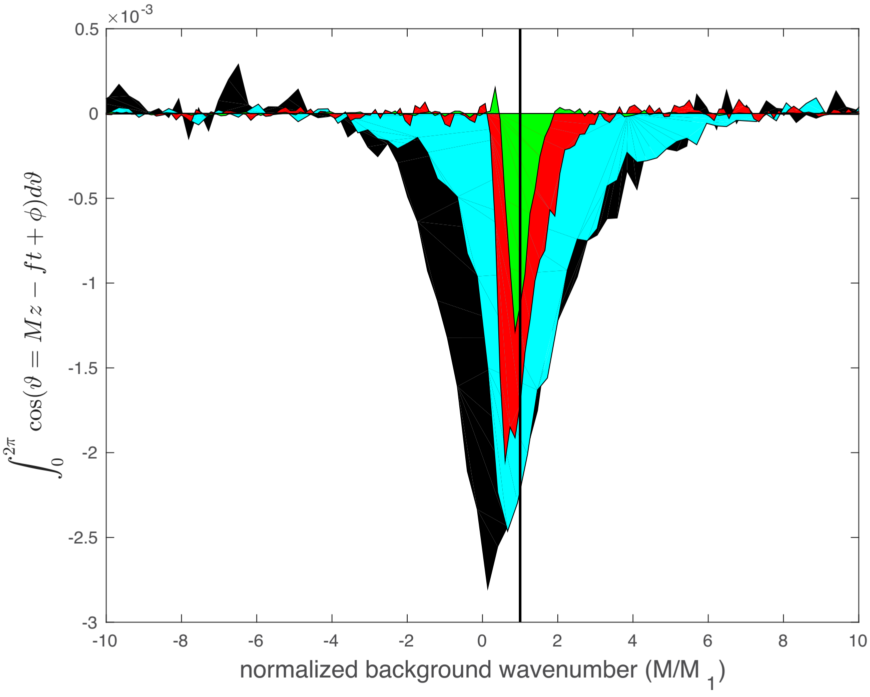

FIG. 8. Phase-averaged energy transfer distributions [(44)], $e_o/e_{\rm GM} = [1, 0.1, 0.01, 0.001]$ (black, cyan, red, and green, respectively). The widths of the distributions vary more than the peak height, consistent with the scaling described in section 4a(2) and appendix D. The vertical line represents the resonance $M_r = f/C_g^z$ associated with the group velocity $C_g^z$ at time $t = 0$.

the half-widths $\gamma_M$ are reasonably well predicted by Polzin and Lvov (2017, their Fig. 9 and our appendix D):

$$\frac{\gamma_M}{M_r} \cong \left[3\pi\left(\frac{\omega}{Nf}\right)^2 e_0 m_* M_r\right]^{1/3}. \qquad (45)$$

This scaling of the resonant well differs from the small-amplitude limit of the kinetic equation, $\gamma \propto e_o/e_o^{\rm GM}$, and the finite-amplitude degradation into the rms Doppler shift, $\gamma \propto (e_o/e_o^{\rm GM})^{1/2}$ (Polzin and Lvov 2017). These differences in scaling underscore the fact that ray tracing is an FM paradigm and the kinetic equation represents nonlinear transfers as an AM process.

Estimates of the mean shear can be obtained by integrating (43) over phase $\vartheta$ (Fig. 8) and subsequently integrating over background wavenumber $M$ (Fig. 9). We anticipate a scaling for the downscale energy transport $\mathcal{P}$ (section 5a) in which $\mathcal{P} = 2\int_f^N \langle \dot{m} \rangle e(m, \sigma) d\sigma \propto e_0^2$. Since $e(m, \sigma) \propto e_0$ and the root-mean-square inertial shear $\mathcal{U}_z^{\rm rms}$ scales as $e_0^{1/2}$, we anticipate $\langle \mathcal{U}_z \rangle / \mathcal{U}_z^{\rm rms}$ to scale as $e_0^{1/2}$. Starting at a level of 0.1 GM, we find a factor of 2 departure from this scaling at oceanic amplitudes (Fig. 9), with larger scale separation factors ss associated with greater departures from the scaling. This factor of 2 decrease is insufficient to overcome the order of magnitude disparity between predicted transports (section 5a) and observations.

Contributions to the mean shear [(43)] can come from either an increasing bandwidth $\gamma_M$ and/or increasing peak probability density. Given that the bandwidth of the probability distribution [(45)] scales as $e_0^{1/3}$, implied in the scaling $\langle u_z \rangle / u_z^{\rm rms} \propto e_0^{1/2}$ is that the peak amplitude of the phase-averaged distributions scale is $e_0^{1/6}$. Indeed, we find a factor of 2 increase in peak probability density as the background increases from 0.001 to 0.1 GM (Fig. 8).

### b. *Moments and correlation functions*

In this subsection, we use the numerical output to quantify lag correlation functions [(37)] (Fig. 10) and the evolving moments in the vertical wavenumber of a test-wave distribution [(28)] (Fig. 11). There are contrasts between the wave turbulence and ray-tracing paradigms. From a wave turbulence perspective, everything is subsumed into the resonant process. From a ray path perspective, the correlation time-scale results from the nonresonant parts of the problem, whereas the mean drift is related to zero encounter frequency in which inertial phase velocity equals internal wave group velocity.

The lag correlation functions (Fig. 10) are suggestive of a two-time-scale process. There is rapid evolution of the time-integrated correlation functions on a short time scale of approximately $1/\langle \omega \rangle$ and a slower evolution on a longer time scale. Note that, although correlations are small at large lag, integration demonstrates these large lags have nonzero contributions. From our discussion of transport metrics linking (37)–(42), we identify the fast time-scale process as the nonresonant response and dispersion about the mean drift. This fast time scale is controlled by the scale separation factor ss [(41)] with greater scale separation leading to diminished transport

Brought to you by MBL/WHOI Library | Unauthenticated | Downloaded 06/09/25 01:56 PM UTC

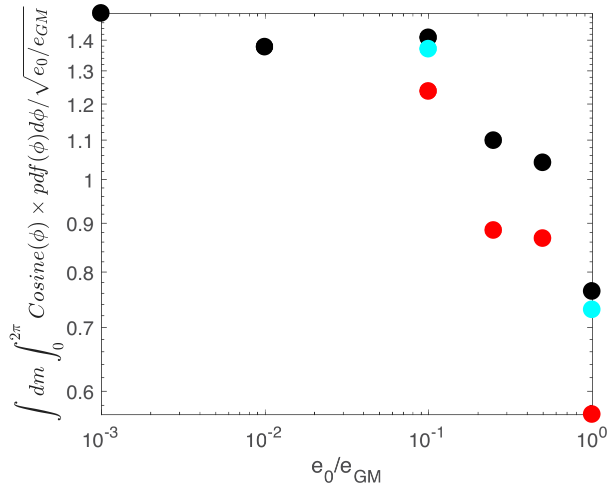

FIG. 9. Normalized version of the mean drift rates [(43)] estimated from the phase distributions in Fig. 7, as a function of $e_o/e_{\mathrm{GM}}$. The normalized values would appear as a constant if $\langle \dot{m} \rangle \propto e_o$. Scale separations ss = [1, $1/\pi$, $\pi$] are visualized in black, cyan, and red, respectively. Greater scale separations imply larger correlation time scales, hence smaller differences between mean drift and correlation time scales, and thus larger departures from the resonant scaling of the mean drift [(36)].

metrics at smaller inertial amplitudes. We intuit the slow time scale to be associated with the resonant response and mean drift. Such contributions at large lags are robust in the sense that we have subtracted the sample mean, consistent with (37). Rescaling $\mathcal{U}_z(t)$ to account for nonstationary statistics does not eliminate the increasing trend in the time-integrated correlation. A possible metric of this time scale is the width of the resonant well [(45)], divided by the mean drift $\langle \dot{m} \rangle$ projected onto the resonant wavenumber $M_r = fm/\omega$. We are unable to further elucidate this long time scale as our simulations terminate before it is resolved.

Deviations from the nominal scalings [(28)] for both the first and second moments are discernible in all model runs (Fig. 11, compare green and red traces). Such departures are much more subtle at small amplitude, and further diagnostics demonstrate that these departures occur in the latter half of the simulations. We suspect deviations from this scaling at small amplitude are related to the use of $(\omega^2 - f^2)^{1/2} = kN/m$ as a dispersion relation associated with the ray (18) rather than the scale-invariant $\omega = kN/m$. We have terminated the analysis such that less than 1% of waves have $\omega < \sqrt{2}f$, but this might not be sufficiently stringent. The deviations at oceanic amplitudes are of greater importance. At oceanic amplitudes, the evolution rates of wavenumber and frequency are of a similar order of magnitude to the wave frequency, with the consequence that the long time approximation in (41) is no longer accurate. That is, we find an inhibition of the second moment when the drift time scale $m/\langle \dot{m} \rangle$ is similar to the correlation time scale. Consistently, larger scale separations ss lead to earlier onset of departures from the nominal scaling at smaller background amplitudes (Fig. 9). The long time limit in which $\langle \omega \rangle$ can be considered to be constant in (41) is known as the Markov approximation, and the suppression of first and second moments occurs in connection with the transition to a non-Markovian limit. That this should impact the second moment is obvious from (41), but the rationale for departures in the mean drift is less obvious. An explanation likely lies in higher-order contributions to the stationary phase analysis in section 3b(2).

### c. Reprise

In this section, we have presented quantitative diagnostics from one-dimensional ray-tracing simulations. This presentation documents that ray theory brings results that differ from the kinetic equation. Scalings for the resonant bandwidth are different, ray tracing has a mean drift absent from the kinetic equation, and dispersion about that mean drift results from a nonresonant process in ray theory. Similar behavior should be recoverable from “kitchen sink” treatments (Henyey et al. 1986; Sun and Kunze 1999b; Ijichi and Hibiya 2017) if those numerics were executed in an appropriate small-amplitude parameter regime.

## 5. Discussion

In this section, we compare a prediction for the rate at which energy is supplied to internal wave-breaking processes with an observational metric. The prediction is an order of magnitude larger than the observations. We then discuss this overprediction in the context of kitchen sink treatments of ray tracing and reflect on the overprediction in the context of extreme scale-separated physics discarded by the ray-tracing approximation.

### a. Energy transport

In Polzin and Lvov (2011, 2017), we noted the tension between an apparent pattern match between observed spectral power laws being in apparent agreement with stationary states of the Fokker–Planck equation (Polzin and Lvov 2011) and this result being inconsistent with what is observationally understood about the energy sources and sinks (Polzin and Lvov 2017; Dematteis et al. 2022), in particular the status of GM76 being a no-flux stationary state due to there being no gradients in action in vertical wavenumber. The ray path perspective moves away from this interpretation so that downscale transport is closed as an advective transport [(28)]. We evaluate (28) by equating the mean drift $\langle \dot{m} \rangle$ with the gradient of the vertical–vertical component of the diffusivity tensor, $\partial D_{33}/\partial m$.

After identifying $n_{\mathbf{p}_1}$ in (24) with the GM76 spectrum, integrating over horizontal azimuth, changing variables from the horizontal wavenumber magnitude to wave frequency, and integrating over vertical wavenumber, in the limit that $m \gg m_*$ and $\sigma \gg f$, (24) becomes

$$D_{33}^{\mathrm{GM}} = k^2 f e_0 m_* \frac{m_1^2}{m_*^2 + m_1^2} \frac{m}{\sigma} \int_f^{\sigma} \frac{2f}{\pi} \frac{d\sigma_1}{\sigma_1^2 \sqrt{\sigma_1^2 - f^2}}$$

$$\to \frac{2}{\pi} \frac{k m^2 e_0 m_*}{N}, \tag{46}$$

to be compared with (25). Here, as in (25), $k$ is the horizontal wavenumber magnitude, $e_0$ is the total energy, $m_*$ is a

Brought to you by MBL/WHOI Library | Unauthenticated | Downloaded 06/09/25 01:56 PM UTC

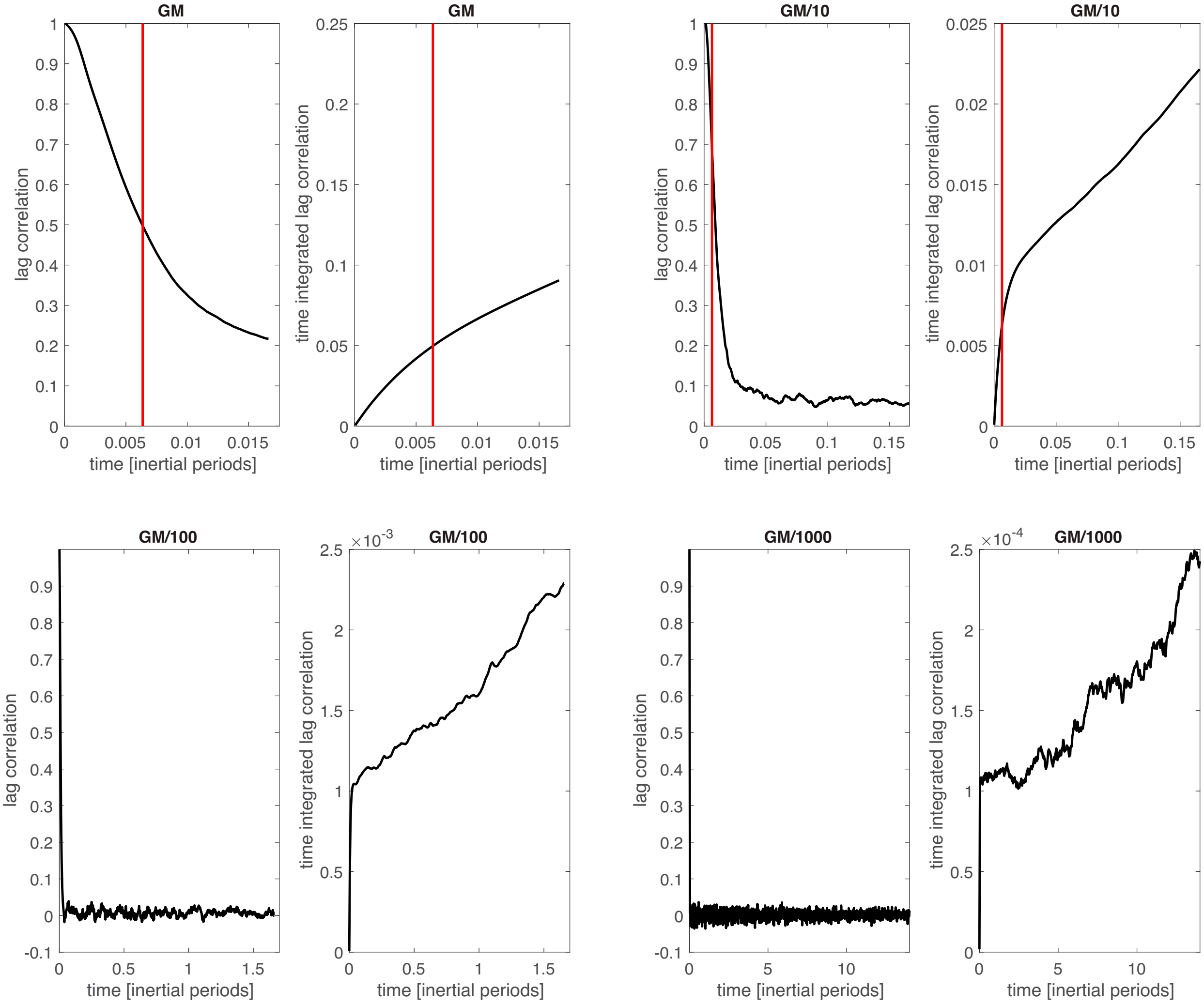

FIG. 10. (left) Lagged autocorrelation functions ($C_{33}$) and (right) their time integrals [(29)]. Upper-left, upper-right, lower-left, and lower-right panels are $10^0$GM, $10^{-1}$GM, $10^{-2}$GM, and $10^{-3}$GM, respectively. The red vertical line represents the wave frequency $\omega$ at $t = 0$, which, in turn, represents the nonresonant correlation time scale. Time integration reveals tertiary contributions at times much larger than the nonresonant correlation time scale. Our hypothesis is that this tertiary contribution comes from the time-changing structure of the resonant well.

bandwidth parameter, and $N$ is the buoyancy frequency. In the GM models, frequency and vertical wavenumber energy spectra are regarded as separable, and normalization constants are incorporated. Thus, in (46), we have $(2f/\pi)\int_f^N d\sigma/\left(\sigma\sqrt{\sigma^2 - f^2}\right) \cong 1$. After including a factor of 2 to account for the two-sided spectral representation, the downscale energy transport is

$$\mathcal{P} = 2\int_f^N \langle \dot{m}\rangle e(m, \sigma)d\sigma = \frac{8}{\pi}\left(\frac{2}{\pi}\right)^2\left(\frac{e_0 m_*}{N}\right)^2 f \log\left(\frac{N}{f}\right) \cong 1.0 \times 10^{-8}(\mathrm{W\,kg^{-1}}), \qquad (47)$$

which, apart from the prefactor of $1.0 \times 10^{-8}$ being an order of magnitude too large, is virtually identical to the finescale parameterization [Polzin et al. 2014, their Eqs. (27) and (40)].

We believe that this one-dimensional treatment is a reasonable representation of high-frequency wave refraction in near-inertial shear. The one-dimensional version dates to the dawn of modern oceanography and is supported by a basic scale analysis of the eikonal relations (McComas and Bretherton 1977; Sun and Kunze 1999a). It is underpinned by the integrable singularity of the inertial peak in the internal wave frequency spectrum and the lack of horizontal velocity gradients in that peak that is encoded in the dispersion relation. Assessments of extreme scale-separated interactions in a nonrotating approximation (Dematteis et al. 2022) assign diffusive transports associated with horizontal and off-diagonal components of the diffusivity tensor that are two orders of magnitude smaller than this advective transport associated with the vertical–vertical component. The nonrotating analysis overestimates the importance of horizontal and off-diagonal transports

Brought to you by MBL/WHOI Library | Unauthenticated | Downloaded 06/09/25 01:56 PM UTC

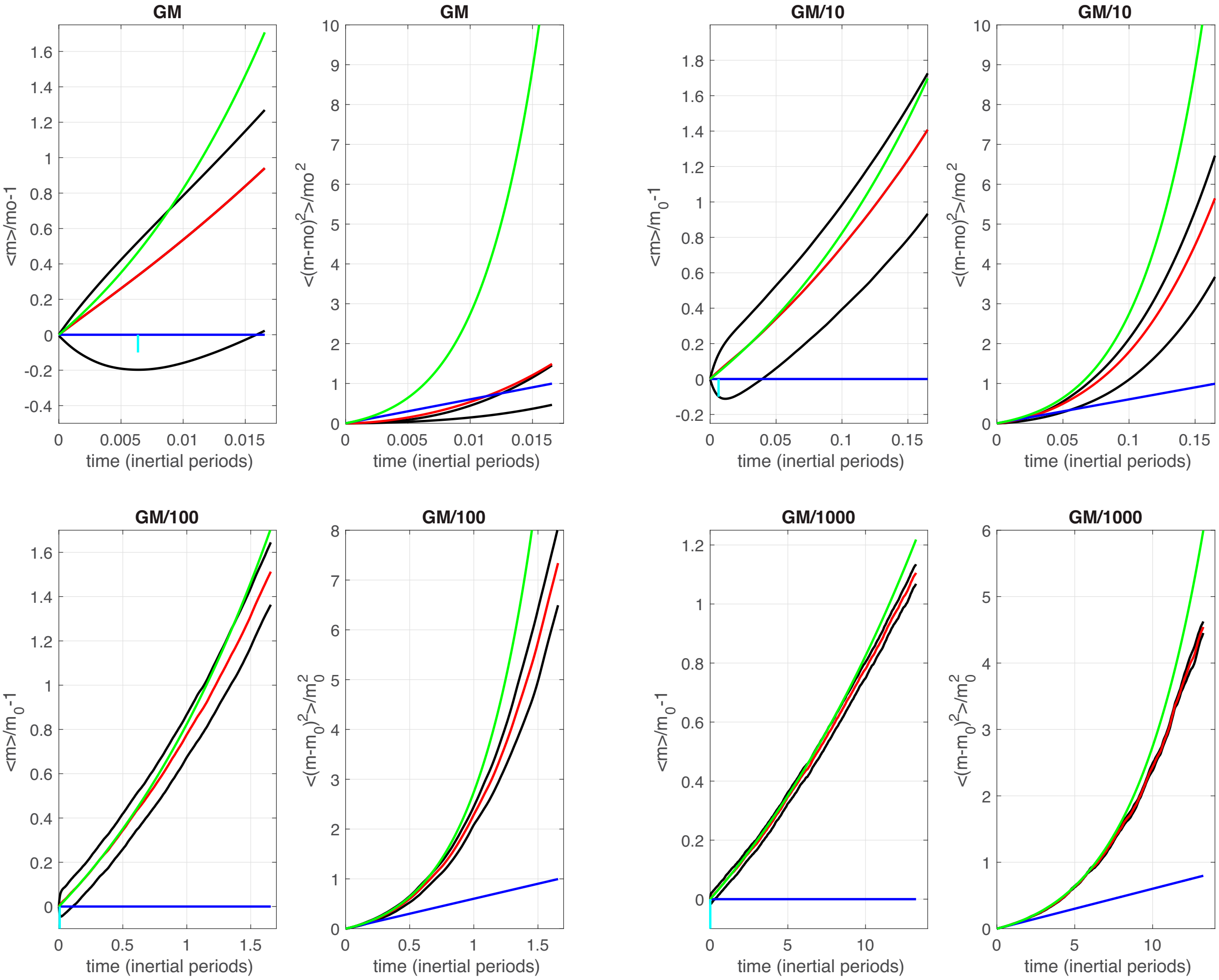

FIG. 11. First and second moments vs time (red and black) with prediction based upon kinetic theory [(28)] (green). The two black lines are ensemble averages conditioned on the sign of the wavenumber tendency (velocity in wavenumber space) at $t = 0$. The red line represents the ensemble average of the conditional moments. The difference between the conditioned estimates relates to the lag correlation time scale [(41)]. The blue line represents a constant diffusivity model. Upper-left, upper-right, lower-left, and lower-right quadrants are $10^0$, $10^{-1}$, $10^{-2}$, and $10^{-3}$ times GM, respectively. (left) The first moment. (right) The second moment. The cyan vertical line represents the inverse wave frequency at $t = 0$.

in a rotating system due to the relative lack of horizontal velocity gradients in the inertial peak. Our model is idealized but not unrealistic.

### b. *Kitchen sink numerics*

Ray methods have also been used in a kitchen sink manner in which test waves are traced in a background consistent with a spectrally filtered version of the Garrett and Munk frequency–vertical wavenumber spectrum (Henyey et al. 1986; Sun and Kunze 1999b; Ijichi and Hibiya 2017). These studies regard the scale separation as a tunable parameter to arrive at advective estimates of downscale transport that, unlike our one-dimensional model, are in sensible agreement with the finescale parameterization. We offer two insights.

The first is that ray tracing is an asymptotic method requiring a scale separation in horizontal wavenumber in addition to the spatial averaging implied in the envelope structure of a wave packet and a small-amplitude assumption (LP). These kitchen sink numerical assessments consistently document sensitivity to the specification of the scale separation and consistently find that the observed finescale metric of energy sourced to turbulent dissipation (Polzin et al. 2014) requires a scale *equivalence*, i.e., the small parameter of an asymptotic expansion must be $\sim O(1)$. This is the hallmark of interactions that are spectrally local in wavenumber and best treated by other methods such as those in Dematteis and Lvov (2021) and Dematteis et al. (2022).

The second insight is that (47) and associated scaling is a fundamental metric that should be recoverable by kitchen sink efforts as a small-amplitude limit using a scale separation that aligns with the assumptions underpinning ray tracing. Departures from this scaling are likely understood as a stochastic

Brought to you by MBL/WHOI Library | Unauthenticated | Downloaded 06/09/25 01:56 PM UTC

forcing that results in "large" amplitude jumps on a "short" time scale over the extent of the resonant well [(45)] that effectively destroys the phase velocity equals group velocity resonance (Polzin and Lvov 2017), parallel to the cleanly articulated Markov approximation for the one-dimensional model captured in (42). The diagnostics presented in section 3 provide the wherewithal to assess this.

### c. *The closure problem*

The Fokker–Planck equation derived from kinetic theory [(14)] represents spectral transports as a diffusive process. The 3D action spectrum of GM76 is independent of the vertical wavenumber, and thus, there is no diffusive transport of action in the vertical wavenumber. Ray theory provides a wave packet ensemble transport [(15)] with an advective contribution. The advective contribution changes the no-flux character obtained with the kinetic equation, as we now have a rationale for the GM76 internal wave spectrum to support turbulent mixing by supplying energy for a wave-breaking process. However, the predicted supply rate [(47)] is an order of magnitude too large.

To interpret why we have arrived at this end result, we find it useful to engage in a high-level discussion of the generic closure problem, motivated by, for example, Orzag (1973) and Holloway and Hendershott (1977), and in textbooks, e.g., Lesieur (1997). In the context of Hamilton's equation for the time evolution of $a_{\mathbf{p}}$, one multiplies by $a^*_{\mathbf{p}}$, multiplies the complex conjugate of Hamilton's equation by $a_{\mathbf{p}}$, subtracts the two equations, and then averages to obtain an evolution equation for the second-order wave action $n_{\mathbf{p}} = a^*_{\mathbf{p}} a_{\mathbf{p}}$ in terms of the third-order correlation function (e.g., Lvov et al. 2012). The process continues iteratively, deriving an equation for the third-order correlation function that involves fourth-order correlations, building up a hierarchy of unclosed equations. If we eliminate all subscripts, coefficients, and summations, the structure can be schematically represented as

$$d\langle\phi\phi\rangle/dt = \langle\phi\phi\rangle + \langle\phi\phi\phi\rangle, \tag{48a}$$

$$d\langle\phi\phi\phi\rangle/dt = \langle\phi\phi\phi\rangle + \langle\phi\phi\rangle\langle\phi\phi\rangle + \langle\phi\phi\phi\phi\rangle^C, \tag{48b}$$

$$\begin{aligned} d\langle\phi\phi\phi\phi\rangle/dt &= \langle\phi\phi\phi\phi\rangle + \langle\phi\phi\rangle\langle\phi\phi\phi\rangle + \langle\phi\phi\phi\phi\phi\rangle^C \\ &\cdots \qquad , \end{aligned} \tag{48c}$$

in which the superscript $C$ denotes the nonreducible cumulant. The intent of a closure is to truncate the hierarchy.

In (decaying) turbulence, the right-hand side of (48b) reads $\langle\phi\phi\rangle\langle\phi\phi\rangle + \langle\phi\phi\phi\phi\rangle^C$. Discarding the fourth-order cumulant in this equation is referred to as the quasi-normal (QN) approximation. This is not a statement that the statistics of turbulence are Gaussian; rather, it is a statement that the fourth-order cumulant can be neglected at all times in comparison to the remaining terms. This approximation leads to a prediction of negative energy in the energy-containing range of the turbulent spectrum (Ogura 1963). Orzag (1973) addressed this by proposing the fourth-order cumulant be approximated as a linear damping term in the third-order equation. This approximation is referred to as the eddy-damped QN (EDQN) approximation: eddy energy (a second-order moment) is not damped; it is the third-order moment that represents energy exchange that is damped. A final approximation, that the damping time scale varies on a time scale much longer than the time over which $\langle\phi\phi\rangle\langle\phi\phi\rangle$ evolves, represents a Markov approximation, and one obtains the EDQN Markovian (EDQNM) approximation.

The parsing of the hierarchy [(48)] in wave turbulence is slightly different. Equation (48) represents the slow time evolution of wave amplitudes rather than the immediate consequence of linear wave propagation. In the long time limit, the third moments become indefinitely large over a vanishingly small subset of the possible interactions. That subset is the resonant manifold (Fig. 1). This long time limit leads to a self-consistent description of nearly resonant interactions, i.e., the broadened kinetic equation [Eq. (2.16)] and mass operator [Eq. (2.18)] of LP. The representation obtained by identifying $\langle\phi\phi\phi\rangle$ with $\langle\phi\phi\rangle\langle\phi\phi\rangle$ and substituting in (48a) is the resonant interaction approximation.

It is from this perspective that we can understand Holloway's commentary (Holloway 1980, 1982) in a brighter light. The early work on internal wave kinetic equations [reviewed in Müller et al. (1986)] took the tack of simply deriving the scattering cross sections and asserting the resonant limit without considering the construction of a broadened kinetic equation. We paraphrase as follows:

1) In constructing a self-consistent kinetic equation, one wants a system of field coordinates for which a simple linear combination results in canonical coordinates. Otherwise, one needs to express the wave basis in a Taylor series expansion in wave amplitude, and a lack of clarity in interpreting the broadened equations will ensue. Lagrangian field coordinates (Olbers 1973; McComas 1975; Meiss et al. 1979, not to be confused with ray path coordinates) require a Taylor series expansion about the assumed smallness of the amplitude to arrive at canonical coordinates.
2) Attempts at deriving a self-consistent internal wave kinetic equation from the standpoint of a stationary observer are doomed to failure for the same reason that afflicted Kraichnan (1959) in the context of 3D turbulence: Doppler shifting of the small scales by the large. Kraichnan (1965) deals with this by effectively using only terms in the scattering cross sections related to pressure and viscosity and thus, in some manner, references Lagrangian estimates of correlation time scales.
3) One really wants to know the time scale $\Gamma^{-1}$ [the inverse resonant bandwidth, Eq. (2.18) of LP] because the closure of the third-order moment [(48b)] ultimately rests upon an assumption that the time integration has converged. Substitution of possible relevant time scales challenges the underpinning assumption that the kinetic equation describes a slow time evolution, but there are only guesses about the relevant time scales. See points 1 and 2 above.

Item 1 is accomplished in Lvov and Tabak (2004): isopycnal field coordinates lead directly to canonical coordinates. Items 2

Brought to you by MBL/WHOI Library | Unauthenticated | Downloaded 06/09/25 01:56 PM UTC

and 3 are addressed in Polzin and Lvov (2017). Using a self-consistent kinetic equation for isopycnal coordinates presented in Lvov et al. (2012), Polzin and Lvov (2017) demonstrate that the resonant bandwidth $\Gamma$ suffers from the Doppler shift defect and, moreover, demonstrate that a frequency renormalization does not alter the transport estimate. We therefore conceived of the one-dimensional ray-tracing model (Polzin and Lvov 2017 and section 2) to investigate. This has led to the articulation of a master equation [(28)] for the ray path formalism (LP), which in turn overpredicts the finescale parameterization metric for downscale transports by an order of magnitude!

We propose the following two-part interpretation for that overprediction.

First, the action conservation of a single packet and the resulting ensemble average [(28)] are incomplete expressions of extreme scale-separated dynamics. The ray-tracing paradigm reveals a phase locking of high-frequency waves with inertial shear along a phase velocity equals group velocity condition (Fig. 2) that implies the creation of statistically inhomogeneous conditions in which regions of large inertial shear host accumulations of high-frequency wave stress (Fig. 7). These conditions are just those that are subject to relaxation by the elastic scattering triad (Fig. 3), which we present as a Bragg scattering process. In Fig. 1, we schematically represent the refractive mechanism of induced diffusion using waves "1" and "B." For a given high-frequency wave $\mathbf{p}_1 = (k, 0, m)$, the Bragg scattering mechanism concerns a wave $\mathbf{p}_2 = (k, 0, -m)$ and a low-frequency wave at $p = (0, 0, 2m)$, skematicized as transfers between waves 1, "2," and "A." The wave stress (momentum flux density) is $u'w' \propto kC_g^z E(\mathbf{p})$ [(7)]. Thus, wave 2 has the opposite sign of energy transfer from the inertial wave than wave 1. Bragg scattering therefore damps the accumulation of wave momentum by transferring wave energy into another high-frequency wave of opposite sign vertical wavenumber, and hence vertical group velocity, at constant horizontal wavenumber.

The importance of this damping can be inferred from the spatially homogeneous kinetic equation. Action balances for the Bragg scattering triad lead to (McComas and Müller 1981a)

$$\frac{\partial[n(\mathbf{p}_1) - n(\mathbf{p}_2)]}{\partial t} = \tau_r^{-1}[n(\mathbf{p}_2) - n(\mathbf{p}_1)], \qquad (49)$$

with $\mathbf{p}_1$ and $\mathbf{p}_2$ interpreted as in Fig. 1. For the GM76 spectrum, the Bragg scattering relaxation time scale $\tau_r$ is equal to the slow induced diffusion time scale (McComas and Müller 1981a), which we have identified as $\partial D_{33}/\partial m$ and demonstrated to be equal to the drift time scale $\langle \dot m\rangle/m$. In short, we intuit that refraction and scattering are exquisitely balanced in this problem. The essence of this, an exponential diminution of the ID coupling, is potentially recoverable using layered media theory (e.g., Fouque et al. 2007).

The result [(49)] is for the spatially homogeneous kinetic equation. Quantifying the coupling and consequent diminishment of downscale transports implies including the Bragg scattering term while integrating along a ray. Methods for incorporating such effects in an ensemble transport equation exist in literature concerning open quantum systems. On an intuitive level, one is trying to describe the interaction of a "system" (the phase velocity–group velocity interaction) with a "bath" (a homogeneous isotropic field of other high-frequency waves), through an "interaction" (Bragg scattering). The system is simply the first-order differential $\dot n(\mathbf{p}_1) = 0$ expression of action spectral density conservation. We present further information about setting up a density matrix from a Hamiltonian perspective in appendix C. *If* the interaction term presents itself as in (49), one has a system of coupled first-order inhomogeneous differential equations:

$$\dot n(\mathbf{p}_1) = [n(\mathbf{p}_2) - n(\mathbf{p}_1)]/2\tau_r^{-1},$$

$$\dot n(\mathbf{p}_2) = [n(\mathbf{p}_1) - n(\mathbf{p}_2)]/2\tau_r^{-1},$$

and an obvious path forward is to solve this first-order inhomogeneous differential equation by using an integrating factor. Physically, this implies integration in time along a ray path. We intuit that a fundamental parameter will be the amount of time a wave packet spends in a single resonance, which depends upon the resonant bandwidth [(45)] and mean drift [(36)], relative to the Bragg relaxation time scale $\tau_r$. This characterizes the ray path formalism's equivalent of an EDQN closure.

Second, the limit of $\tau \to \infty$ as the lower bound of integration in (37) is the signature Markov approximation. Whether such a replacement is reasonable, though, requires justification. The results of our one-dimensional model at oceanic amplitudes suggest otherwise, but this requires defining the relevant time scale for the sake of comparison. We believe this time scale to be $m/\langle \dot m\rangle$ since the wave frequency enters into the lag autocorrelation time scale [(42)] and vertical wavenumber and frequency are related through the dispersion relation. This is a by-product of the ad hoc construction of a spatial scale separation [(20)] criterion in our one-dimensional model to supplant a dynamically self-consistent specification of the wave packet envelope. On the other hand, if downscale transports are reduced by an order of magnitude by Bragg scattering, which is entirely reasonable considering the disparity between the prediction [(47)] and community wisdom articulated in Polzin et al. (2014), then an extended one-dimensional closure could fit within the domain of an EDQNM scheme.

A schematic ordering of relevant time scales at oceanic amplitudes is contained in Table 2 rendered in Fig. 12. After averaging over mesoscale eddy time scales, we represent the long time variations in action spectral density as seasonal. Spectral transports occur within a phase velocity–group velocity velocity resonance that has an event time scale $\tau_{\rm event}$ which we estimate as the ratio of the resonant bandwidth $\gamma_M$ [(45)] and the projection of the average drift rate $\langle \dot m\rangle$ onto the inertial field, $\dot M_r$, with $\dot M_r/M_r = 2\langle \dot m\rangle/m$; see section 2. Mean drift $\tau_i$ and Bragg scattering $\tau_r$ operate on identical slow ID time scales. At oceanic amplitudes, these are somewhat shorter time scales than those characterizing resonant events. A scale separation between $\tau_{\rm event}$ and $\tau_{\rm i}$ implies the creation of local conditions that are vertically anisotropic and prone to relaxation by Bragg scattering. At oceanic amplitudes, mean drift

Brought to you by MBL/WHOI Library | Unauthenticated | Downloaded 06/09/25 01:56 PM UTC

TABLE 2. Time scale definitions for Fig. 12.

| | | |
|---|---|---|
| $\Gamma$ | | Resonant bandwidth (fast ID; rms Doppler shift) |
| $\tau_c$ | $\dfrac{\int_{t-\tau}^{t}\langle[\dot{m}(t)-\langle\dot{m}(t)\rangle][\dot{m}(t-\tau)-\langle\dot{m}(t-\tau)\rangle]\rangle d\tau}{\langle[\dot{m}(t)-\langle\dot{m}(t)\rangle]^2\rangle}$ | Correlation time scale |
| $\tau_i$ | $\dfrac{m}{\langle\dot{m}\rangle}$ | Mean drift (slow ID) |
| $\tau_r$ | $\tau_i$ | Bragg scattering |
| $\tau_{\mathrm{event}}$ | $\dfrac{1}{2}\dfrac{m}{\dot{m}}\times\left[3\pi\left(\dfrac{\omega}{Nf}\right)^2 e_0 m_* M_r\right]^{1/3}$ | $\dfrac{\text{width of resonant well}}{\text{mean drift projected onto } M}$ |

rates are comparable to the correlation time scale $\tau_c$ = ss/$\langle\omega\rangle$ for nonresonant forcing and challenge a Markov approximation upon which a diffusive closure is predicated. The bandwidth of the self-consistent kinetic equation is the inverse of the fast ID time scale, $\Gamma$.

We are aware of rigorous proof (Deng and Hani 2021) that fourth-order cumulants are subleading-order terms in the expansion [(48)] under weak linearity for spatially homogeneous systems. Our efforts demonstrate that there are fundamental differences in the statistics of the resonances accumulated along ray paths rather than as a stationary observer. This line of argument is further sustained by the finding in Polzin and Lvov (2017) that the resonant bandwidth $\Gamma$ tends to the rms Doppler shift at finite amplitude, while the underpinning dynamics of ray tracing are to represent the variations in the Doppler shift. Individually, Bragg scattering and inertial phase velocity–internal wave group velocity resonances are, in the ray path analysis, the leading-order extreme scale-separated processes and have time scales shorter than those associated with local interactions that we intuitively characterize as having a dimension greater than one. Our proposition is that these leading-order extreme scale-separated processes are coupled with a resulting diminishment of transports. We draw upon 3D turbulence to present this coupling as a fourth-order cumulant in the context of an EDQNM closure. We regard this as a physically reasonable justification for the 1D system in the face of the rigorous 3D proof in Deng and Hani (2021).

Finally, we note that there is an indirect analogy concerning the propagation of electrons in a lattice known as Anderson

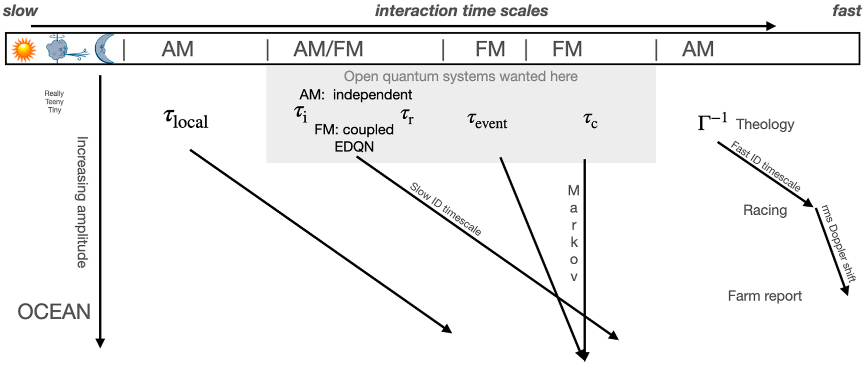

FIG. 12. A schematic ordering of time scales. Time scales decrease from left to right, and wave amplitude increases from top to bottom. The shortest time scale is associated with the resonant bandwidth $\Gamma^{-1}$ and can be identified as the fast ID time scale of kinetic theory. At oceanic amplitudes, this bandwidth degenerates into the rms Doppler shift. The phase velocity equals group velocity $\tau_I$, and Bragg scattering resonances $\tau_r$ operate on similar time scales and can be identified as the slow ID time scale of kinetic theory. These interaction time scales decrease with increasing wave amplitude. A correlation time scale $\tau_c$ associated with nonresonant forcing provides the shortest time scale for the ray-tracing simulation. At oceanic amplitudes, the interaction time scales are similar to the correlation time scales and provide an issue for the closure of ensemble-averaged transports. At oceanic amplitudes, the breadth of the phase velocity equals group velocity resonance in the spectral domain is such that ensemble average transit times through the resonance $\tau_{\mathrm{event}}$ are longer than the drift time scale $\tau_i$. The longest depicted time scale relates to climatological patterns of forcing. The characterization of AM denotes the AM basis of kinetic theory; FM applies to the FM paradigm of ray tracing (Polzin and Lvov 2017). The time scale $\tau_{\mathrm{local}}$ represents local interactions in the kinetic equation (Dematteis et al. 2022).

Brought to you by MBL/WHOI Library | Unauthenticated | Downloaded 06/09/25 01:56 PM UTC

localization. As the impurities in that lattice become greater, electrical resistance increases in proportion. When the impurities reach a density of two per unit wavelength of the electron, the material suddenly becomes an electrical insulator. Our assessment of the internal wave problem has the same character. A path integral assessment leads us to a description that predicts downscale energy transfer in an order of magnitude greater than supported by observations. We forward the hypothesis that the inclusion of Bragg scattering physics associated with a background inertial wavefield at half the vertical wavelength of the high-frequency internal wave will similarly shut down mean drifts to higher wavenumber. Localization occurs in many different physical systems (Lagendijk et al. 2009) with similar concerns about the dimensionality of the system impacting the potential for localization (e.g., Sheng and van Tigglen 2007).

## 6. Summary

As we look back over the landscape of this endeavor, what we have is a well-established metric for ocean mixing (Polzin et al. 2014) which, prior to Dematteis et al. (2022), did not have a first principles support. At best, the finescale parameterization was underpinned by a heuristic description as an advective spectral closure (Polzin 2004a) in the context of an energy transport equation that eschews action conservation. Application of classical wave turbulence to extreme scale-separated interactions arrives at a Fokker–Planck equation expressing wave action diffusion that predicts no downscale spectral transports in vertical wavenumber [(24)]. This result is a consequence of the fact that the GM 3D action spectrum is independent of vertical wavenumber in its high-wavenumber power-law regime: there are no gradients of action to support a diffusive transport. Application of ray path techniques in LP arrives at a combined advection/diffusion transport [(28)] that supports downscale vertical wavenumber transports of energy and action for the GM spectrum. In this paper, we utilize an idealized representation of high-frequency oceanic internal waves propagating in a background of inertial waves to obtain concrete closures for the ray path formulation. These closures recover the wave turbulence kinetic equation diffusivity and identify the mean drift of wave packets as the gradient of the kinetic equation diffusivity in vertical wavenumber. This represents qualitative progress in reconciling observations with theory. However, predictions for energy transport associated with the mean drift are an order of magnitude larger than the observations. Ray-tracing simulations are conducted to assess these closures. There is a tendency for the mean drift to be reduced from these small-amplitude scalings at oceanic amplitude, but this reduction is insufficient to ameliorate the glaring order of magnitude discrepancy between prediction and observation. There is a wealth of information available in the ray-tracing simulations concerning phase locking and correlation time scales that enable us to effectively order the time scales of a cumulant hierarchy [(48a)–(48c)].

Meditation upon this hierarchy in the context of 3D turbulence produces some parallels. The distinction between wave turbulence and ray path techniques invites a comparison between Eulerian (Kraichnan 1959) and Lagrangian (Kraichnan 1965) formulations of 3D turbulence, with Eulerian formulations being prone to contamination by Doppler shifting. The wave kinetic equation represents nonlinear interactions as an amplitude modulation of spatially infinite plane waves and predicts a very rapid adjustment of a spike inserted into an otherwise smooth spectrum (McComas 1977). At oceanic amplitudes, this adjustment time scale tends to an aphysical rms Doppler shift (Polzin and Lvov 2017). The ray path derivation invokes a Wigner transform that integrates the evolution of this spectral spike with its interaction partners and explicitly represents *variations* in Doppler shifting as the underpinning dynamics. In 3D turbulence, the change from Eulerian to Lagrangian perspectives changes predicted power laws from $k^{-3/2}$ and $k^{-5/3}$. In the internal wave problem, the concept of ensemble averaging wave packets following ray trajectories provides motivation to include a mean drift term in the transport equation. This is a qualitative difference, and revised estimates of downscale transport overshoot the mark by an order of magnitude. These quantitative differences are potentially resolved by parallels concerning the role of fourth-order cumulants. In 3D turbulence, fourth-order cumulants are understood to provide a systematic damping of downscale transports associated with third-order terms (Orzag 1973). Here, we propose a Bragg scattering process that reduces the downscale transports associated with a phase velocity–group velocity resonance. We interpret Bragg scattering as a fourth-order cumulant playing the role of a third-order damping. We find that Bragg scattering and the mean drift have essentially identical time scales.

We identify the Bragg scattering process in terms of the time evolution of the correlation between the two high-frequency wave amplitudes having similar horizontal wavenumber and oppositely signed vertical wavenumber. Incorporating such effects into a wave packet action balance and deriving a corresponding transport equation are subjects of current research. Similarly, the dynamics that control the envelope structure of the wave packet and interactions of a wave packet with the residual flow associated with the packet's envelope structure (Bühler and McIntyre 2005) have been discarded in the ray-tracing paradigm (Gershgorin et al. 2009). Accounting for the latter requires loosening the specification of layerwise constant potential vorticity (Lvov and Tabak 2004) which is a key piece of isopycnal coordinates representing a canonical Hamiltonian system. This, again, is a topic of current research.

*Acknowledgments.* K. L. P. and Y. V. L. (Grant N000141-712852) gratefully acknowledge support from the Office of Naval Research for this project.

*Data availability statement.* No data were created for this paper.

Brought to you by MBL/WHOI Library | Unauthenticated | Downloaded 06/09/25 01:56 PM UTC

## APPENDIX A

### Horizontal Stress–Strain Relations

We start thinking about the coupling of internal waves with mesoscale eddies in an extreme scale-separated limit by assuming a quasigeostrophic scaling for the eddies:

$$S_n = U_x - V_y$$

$$S_s = V_x + U_y$$

$$\zeta = V_x - U_y$$

$$\Delta = U_x + V_y = 0,$$

where $S_n$ and $S_s$ are the components of the deformation rate of the strain tensor, $\zeta$ is the relative vorticity, and $\Delta$ is the horizontal divergence, assumed small.

Horizontal stresses are the projection of the horizontal wavevector onto the deformation tensor [Fig. 1 of Polzin (2010)]. We use the polarization relations [(2)] to make this explicit in the energy equation:

$$\begin{aligned}
-\overline{u'u'}U_x - \overline{v'v'}V_y &= -(kC_g^x - lC_g^y)\frac{aa^*}{\omega}S_n/2 \\
&= -(k^2 - l^2)\frac{N^2}{m^2\omega^2}S_n/2 \\
-\overline{u'v'}U_y - \overline{v'u'}V_x &= -(kC_g^y - lC_g^x)\frac{aa^*}{\omega}S_s/2 \\
&= -(kl)\frac{N^2}{m^2\omega^2}S_s. \qquad \text{(A1)}
\end{aligned}$$

Assuming that the time dependence of the horizontal wavenumber exceeds that of the background gradients along a ray, upon differentiation with respect to the time of the eikonal [(5)], one (Jones 1969) arrives at

$$[\ddot{k}, \ddot{l}] = [k, l](S_n^2 + S_2^2 - \zeta^2), \qquad \text{(A2)}$$

which implies the exponential growth and decay of horizontal wavenumber along the ray if the rate of strain dominates the relative vorticity and oscillatory solutions otherwise. While one might quibble regarding the amount of time the deformation rate of strain can be considered constant along the ray, one has arrived at an intuitive understanding of horizontal stress and horizontal strain correlations. See Figs. 3 and 4 and Figs. 4 and 5 of Polzin (2010) for observations documenting the horizontal stress–strain and vertical stress–shear relations, respectively.

We next want to enhance our dynamical understanding, which we find in appendix B.

## APPENDIX B

### Parsing Extreme Scale-Separated Wave–Mean Interactions

In Polzin and Lvov (2011), we provide a catalog of parametric spectral fits to deep ocean vertical wavenumber and frequency data and articulate the existence of, in comparison to the universal model (Munk 1981), regional variability. The parameters include power laws, vertical wavenumber bandwidth, and amplitude. We also examine seasonal variability in time series of near-inertial and high-frequency bands. We forward the hypothesis that the resulting spatial–temporal variability reflects the regional variability in the forcing mechanisms: winds, tides, and eddies, mediated by regional variations in nonlinear transfers. We then attempted to align that parametric variability with spatial–temporal variability in the forcing mechanisms. We also articulate a prioritization of efforts to understand the regional variability: that the leading-order ignorance concerns nonlinear transformations, specifically the issue of Doppler shifting in induced diffusion and the obvious importance of hitherto neglected transports in horizontal wavenumber associated with "local interactions."

This effort has required us to express the fundamental differences between ray tracing, which deals explicitly with Doppler shifting, and the kinetic equation, which has a Doppler shift defect in the induced diffusion limit. The most fundamental difference is that the kinetic equation represents a system of amplitude-modulated plane waves and ray tracing represents a system in which the amplitude (the action spectral density) is constant and the constituents of wave phase are modulated according to the eikonal relations.

This effort results in original developments concerning the bandwidth of amplitude-modulated vs phase-modulated signals, which have corollaries as AM and FM signals on your radio (Cohen and Lee 1990; Polzin and Lvov 2017). This effort also produces original results concerning mean drift terms in wave packet ensemble average representations of action transport, which returns an absurd prediction of 10 times too much mixing (section 5a). This absurdity then launches us into a discussion of representing Bragg scattering as an eddy-damped quasi-normal Markovian process to cancel that absurdity. This is an affirmation that the Bragg scattering time scale is the leading-order (shortest time scale) nonlinear process with its primary mission being a return to vertically isotropic conditions. This leaves local interactions operating in both vertical and horizontal wavenumber (Dematteis et al. 2022) and the parametric subharmonic instability (MacKinnon et al. 2013; Olbers et al. 2020) as the leading players affecting downscale energy transport by nonlinear wave–wave interactions.

Given a geometric understanding of energy exchanges via internal wave stress–mesoscale strain relations (appendix A), the implications of our results for the coupling of mesoscale eddies and internal waves are greatly clarified.

In Müller (1976), mesoscale eddy–internal wave coupling is represented using a single-scale eddy and a multichromatic wavefield. That analysis starts from an expression of action spectral density conservation and introduces small perturbations in wave phase speed associated with ray tracing at higher order. The zeroth-order wavefield is assumed to be homogeneous and isotropic, with perturbations being returned to an isotropic state by nonlinear wave–wave

Brought to you by MBL/WHOI Library | Unauthenticated | Downloaded 06/09/25 01:56 PM UTC

interactions in a relaxation time-scale approximation. It is this relaxation process that makes energy exchanges between the two systems permanent: otherwise, the wave packet can wander around about its initial trajectory with no net exchange in the single-scale eddy field. Energy exchanges in this problem concern internal wave momentum (i.e., wave stresses) acting against the mesoscale gradients. The key role of the nonlinearity is to return the momentum flux perturbations to an isotropic state. For the vertical stresses coupling with thermal wind shear, this concerns Bragg scattering on a fast time scale as the sign of the vertical wavenumber is flipped and the horizontal wavenumber is unchanged. For horizontal stresses coupling with the mesoscale rate of strain, changing the sign of the horizontal wavenumber does not change the sign of the horizontal stress, e.g., (A1) and Fig. 1 of Polzin (2010). Relaxing perturbations in horizontal stress requires modifying either horizontal azimuth or horizontal wavenumber magnitude. Modifying horizontal wavenumber magnitude is likely to be more effective as nonlinear interactions have a distinct tendency to be colinear with parallel or antiparallel horizontal wavevectors [Fig. 2 of Dematteis and Lvov (2021)]. Intuitively, the time scale for modifying horizontal wavenumber magnitude is associated with downscale transports in the finescale parameterization, which this contribution documents as an order of magnitude longer than the Bragg scattering time scale.

Changes in momentum flux following changes in wavenumber magnitude at the nominal finescale parameterization imply a far less efficient relaxation process than in the vertical coordinate associated with Bragg scattering. This represents a plausible hypothesis for why the vertical stress–thermal wind shear coherences are typically smaller than the horizontal stress–mesoscale rate of strain coherence estimates; see Figs. 3 and 4 and Figs. 4 and 5 of Polzin (2010). See section 5.2 and Figs. 42 and 43 of Polzin and Lvov (2011) for estimates of the energy source functions using formulas in Müller (1976). These estimates are consistent with the conclusions of Polzin (2010) that mesoscale eddy–internal wave coupling, amplifying a pre-existing wavefield, is the dominant source mechanism south of the Gulf Stream. The tertiary forcing is plausibly related to energy flux divergences associated with low-mode internal tides and low-mode near-inertial waves sourced from the north of the Gulf Stream (Zhao et al. 2016; Alford and Zhao 2007).

Muller's derivation is incomplete in that it is an assessment of higher-order balances in a perturbation expansion of action conservation in a multichromatic wavefield. This action balance is only the leading-order expression for a single wave packet at its carrier frequency; see section 3.2 of LP. The leading-order wave packet balance neglects the residual flow associated with the momentum flux divergences on the envelope scale and the potential for the wave to interact with its envelope structure. The wave packet structure carries information about a potential vorticity anomaly (Bühler and McIntyre 2005) that directly concerns whether/how this coupling interacts with deformation scale eddies (Arbic et al. 2013) to possibly truncate an enstrophy cascade regime. The issue of potential vorticity laundering in the ocean interior is fundamental to understanding global ocean behavior on long time scales (e.g., Rhines and Young 1982; Treguier et al. 1997) and needs to be explored.

A second line of inquiry, distinct from Müller (1976), casts the coupling as a single internal wave interacting with a multiscale eddy field. This interpretation originates in Watson (1985) and appears, most lately, in Savva and Vanneste (2018), Kafiabad et al. (2019), Dong et al. (2020), Savva et al. (2021), Dong et al. (2023), and Cox et al. (2023). The key concept in the ray-tracing limit is decorrelation and dispersion of wavenumber [(9)] and, following statements about action conservation in Bretherton (1966), energy exchange associated with net trends in intrinsic frequency. We point out above how problematic the action conservation assumption is with regard to Bragg scattering acting on a fast time scale. The kinetic equations and wave packet ensemble action transport expressions in this body of literature are subject to the same criticisms as the wave–wave interaction problem addressed here: kinetic equations can suffer from Doppler shift defects for extreme scale-separated interactions and wave packet ensemble-averaged action transport equations are generically missing a drift term associated with inhomogeneity in the spectral domain. Our interpretation of the net drift term is that of a resonant interaction. This is a plausible interpretation of a coherent feature analysis of Tom Sanford's original Mid-Ocean Dynamics Experiment data (Polzin 2008; Sanford 1975) originally parsed as downward near-inertial wave propagation associated with local atmospheric forcing (Leaman and Sanford 1975): The three-dimensional wavevector resulting from the coherent feature analysis implies a westward group velocity of 1.5 cm $s^{-1}$ that roughly matches the 2 cm $s^{-1}$ westward phase velocity of the Mid-Ocean Dynamics Experiment (MODE) eddy (McWilliams 1976).

Theoretical developments appear to be wanting an empirical ground truth parallel to the "10 times too much mixing" that motivated our work on the induced diffusion problem. Idealized numerical simulations in realistic geometries such as Yang et al. (2023) are a start. However, there is a wealth of ocean observations to test such ideas that begin with the Mid-Ocean Dynamics Experiment (Leaman and Sanford 1975), the internal wave experiment (Briscoe 1975; Frankignoul and Joyce 1979), PolyMODE I and II (Ruddick and Joyce 1979), and the local dynamics experiment of PolyMODE III (Brown and Owens 1981; Polzin 2010), all obtained four decades ago. Section 5.2 of Polzin and Lvov (2011) summarizes the observational metrics for mesoscale eddy–internal wave coupling, and section 3 provides a catalog of parametric fits to frequency and vertical wavenumber spectra that document regional variability in the background internal wave spectrum. A focal point of future theoretical developments should be on whether an assumption of small perturbations to wave phase speed is accurate over the energy-containing part of the vertical wavenumber spectrum at the bandwidth parameter $j_*$,

Brought to you by MBL/WHOI Library | Unauthenticated | Downloaded 06/09/25 01:56 PM UTC

which is characteristically $O(10)$, rather than assuming a mode-1 character and that one-size-fits-all.

## APPENDIX C

### Bragg Scattering along a Ray Path

This begins with Hamilton's equation for the evolution of wave amplitude:

$$i\dot{a}_p = \frac{\delta\mathcal{H}}{\delta a_p^*} \quad \text{and} \quad i\dot{a}_p^* = -\frac{\delta\mathcal{H}}{\delta a_p}$$

$$\mathcal{H} = \int dp_1 dp_2 A(p_1, p_2) a_{p_1} a_{p_2}^*. \qquad \text{(C1)}$$

In order to promote this from the status of simple conjecture, we point the reader to a step-by-step derivation of ray tracing and associated action density conservation presented in LP using an extreme scale-separated Hamiltonian structure. The underpinning assumptions are that (i) there are three waves, one of which has much larger amplitude than the others; (ii) the small-amplitude waves have similar frequencies that are both greater than that of the large amplitude wave; and (iii) the small-amplitude waves have significantly greater *horizontal* wavenumber than the large amplitude wave. Note that the specification on wave frequency conditions the aspect ratio ($k/m$) of the waves. No constraint on vertical wavenumber is implied. Thus, both phase velocity equals group velocity and Bragg scattering resonances in Fig. 1 are retained. This reduces the Hamiltonian density [Eq. (3.12) of LP] to a manageable

$$A(\mathbf{p}_1, \mathbf{p}_2) \cong \sigma_{\mathbf{p}}\delta(\mathbf{p}_1, \mathbf{p}_2) + i\frac{1}{2}\frac{\sigma}{N}\Upsilon_z(\text{A or B}) + \frac{1}{2}\frac{\sigma}{\Pi_0}\hat{\Pi}(\text{A or B}). \qquad \text{(C2)}$$

This setup applies to both resonances, which we have indicated by replacing the arguments of $\Upsilon_z/N$ and $\hat{\Pi}/\Pi_0$ with (A or B).

The factors $\Upsilon_z/N$ and $\hat{\Pi}/\Pi_0$ are the Fourier coefficients describing the vertical shear and isopycnal separation variability (what the oceanographic community refers to as "strain") as vertical gradient analogs of kinetic and potential energy. Ray tracing and action spectral density conservation are obtained by operating on the evolution [(C3)] with a Wigner transform and subsequent Taylor series expansion that focuses upon the B half of the spectral domain. Although the Bragg resonance A and the group velocity–phase velocity resonance B imply an evaluation of the Fourier coefficients at vastly different vertical wavenumber magnitudes, the oceanic vertical wavenumber spectrum for these vertical gradients is independent of vertical wavenumber in its power-law subrange. Thus, the Fourier coefficients at these dissimilar scales have similar magnitudes.

The next step is to derive an evolution equation for the time evolution of the correlation function $N_{1,2} = \langle a(\mathbf{p}_1)a^*(\mathbf{p}_2)\rangle$, in which $a(\mathbf{p})$ are the canonical amplitudes at wavenumbers $\mathbf{p}_1$ and $\mathbf{p}_2$:

$$i\dot{N}_{1,2} = \int (A_{3,\mathbf{p}_1} N_{3,\mathbf{p}_2} - A_{\mathbf{p}_2,3} N_{\mathbf{p}_1,3}) d3, \qquad \text{(C3)}$$

with wavenumber "3" representing a variable of integration. This permits filling out both diagonal and off-diagonal elements of a density matrix. The diagonals represent ray tracing, and the off-diagonals represent transition probabilities.

## APPENDIX D

### The Resonant Bandwidth for Ray Tracing

This appendix repeats an argument in Polzin and Lvov (2017) that results in a scaling for the resonant bandwidth of ray-tracing $\gamma_M$. For a single-wave background, the amplitude of the test-wave response can be estimated from the eikonal relation:

$$\frac{d^g m}{dt} = -kU_z \cos(Mz - ft + \phi). \qquad \text{(D1)}$$

In the off-resonant case, ray trajectories are perturbed by only small amounts from straight lines. Thus, $z = \int C_g^z dt \cong C_g^z(t = 0)t$, and integration of (D1) provides

$$[m - m(t = 0)]^2 = \frac{1}{2}\frac{k^2 U_z^2}{(MC_g^z - f)^2}. \qquad \text{(D2)}$$

This obviously fails at resonance, for which $MC_g^z = f$.

"Near" resonance we consider the happy state in which $MC_g^o - f = 0$ and perturbations in vertical wavenumber sufficiently small as to expand the group velocity in a Taylor series:

$$\frac{d^g m'}{dt} \cong -kU_z \cos\left(MC_g^o \frac{2}{m_o}\int m' dt\right). \qquad \text{(D3)}$$

With $\phi = 0$ and an initial condition that $m'(t = 0) = 0$,

$$m \cong -kU_z t,$$

so that an iterative solution to (D3) suggests

$$\frac{d^g m'}{dt} = -kU_z \cos(MC_g^o kU_z t^2/m_o).$$

We recognize that the implication for the next iterate is one of growth until the argument of the cosine function attains a value of $\pi/2$:

$$\tau_{\text{growth}} = \left(\frac{\pi}{2}\frac{m_o}{MC_g^o kU_z}\right)^{1/2},$$

so that the root-mean-square deviation can be estimated as the product of the amplitude $kU_z$ and this time scale:

$$[m - m(t = 0)]^2 \cong \left(\frac{\pi m_o kU_z}{2f}\right), \qquad \text{(D4)}$$

which provides an effective stepping stone to define the resonance bandwidth in the higher dimensional problems.

Brought to you by MBL/WHOI Library | Unauthenticated | Downloaded 06/09/25 01:56 PM UTC

In Polzin and Lvov (2017), this is accomplished by casting the left-hand side of (D4) as a bandwidth $\gamma_m^2$ and noting that the projection of this bandwidth onto the background field at resonance $f/M = -(kN/m^2)$ implies

$$\frac{\gamma_m}{\gamma_M} = \frac{dm}{dM} = -\frac{\omega}{2f}.$$

The next step is to scale the background shear of a single wave $U_z$ with the shear associated with the resonance $U_z \leftarrow [\gamma_M M^2 e_k(M)]^{1/2}$, obtaining the GM spectrum:

$$\frac{\gamma_M}{M} = \left[3\pi\left(\frac{\omega}{Nf}\right)^2 e_o m_* M\right]^{1/3}. \tag{D5}$$

There are parallels with the stationary phase calculation of section 3b(2), but we have not been able to elevate this argument beyond a scaling estimate.

## REFERENCES

Alford, M. H., and Z. Zhao, 2007: Global patterns of low-mode internal-wave propagation. Part I: Energy and energy flux. *J. Phys. Oceanogr.*, **37**, 1829–1848, https://doi.org/10.1175/JPO3085.1.

Andrews, D. G., J. R. Holton, and C. B. Leovy, 1987: *Middle Atmosphere Dynamics*. Academic Press, 489 pp.

Arbic, B. K., K. L. Polzin, R. B. Scott, J. G. Richman, and J. F. Shriver, 2013: On eddy viscosity, energy cascades, and the horizontal resolution of gridded satellite altimetry products. *J. Phys. Oceanogr.*, **43**, 283–300, https://doi.org/10.1175/JPO-D-11-0240.1.

Bender, C. M., and S. A. Orszag, 1978: *Advanced Mathematical Methods for Scientists and Engineers*. McGraw-Hill, 593 pp.

Bretherton, F. P., 1966: The propagation of groups of internal gravity waves in a shear flow. *Quart. J. Roy. Meteor. Soc.*, **92**, 466–480, https://doi.org/10.1002/qj.49709239403.

——, 1969: Momentum transport by gravity waves. *Quart. J. Roy. Meteor. Soc.*, **95**, 213–243, https://doi.org/10.1002/qj.49709540402.

Briscoe, M. G., 1975: Preliminary results from the trimoored internal wave experiment (IWEX). *J. Geophys. Res.*, **80**, 3872–3884, https://doi.org/10.1029/JC080i027p03872.

Brown, E. D., and W. B. Owens, 1981: Observations of the horizontal interactions between the internal wave field and the mesoscale flow. *J. Phys. Oceanogr.*, **11**, 1474–1480, https://doi.org/10.1175/1520-0485(1981)011<1474:OOTHIB>2.0.CO;2.

Bühler, O., and M. E. McIntyre, 2005: Wave capture and wave–vortex duality. *J. Fluid Mech.*, **534**, 67–95, https://doi.org/10.1017/S0022112005004374.

Cohen, L., and C. Lee, 1990: Instantaneous bandwidth for signals and spectrogram. *Proc. IEEE Int. Conf. Acoustics Speech Signal Process*ing, Albuquerque, NM, Institute of Electrical and Electronics Engineers, 2451–2454, https://doi.org/10.1109/ICASSP.1990.116086.

Cox, M. R., H. A. Kafiabad, and J. Vanneste, 2023: Inertia-gravity-wave diffusion by geostrophic turbulence: The impact of flow time dependence. *J. Fluid Mech.*, **958**, A21, https://doi.org/10.1017/jfm.2023.83.

Dematteis, G., and Y. V. Lvov, 2021: Downscale energy fluxes in scale-invariant oceanic internal wave turbulence. *J. Fluid Mech.*, **915**, A129, https://doi.org/10.1017/jfm.2021.99.

——, K. L. Polzin, and Y. V. Lvov, 2022: On the origins of the oceanic ultraviolet catastrophe. *J. Phys. Oceanogr.*, **52**, 597–616, https://doi.org/10.1175/JPO-D-21-0121.1.

——, A. Le Boyer, F. Pollman, K. L. Polzin, M. H. Alford, C. B. Whalen, and Y. V. Lvov, 2024: Interacting internal waves explain global patterns of interior ocean mixing. *Nat. Commun.*, **15**, 7468, https://doi.org/10.1038/s41467-024-51503-6.

Deng, Y., and Z. Hani, 2021: Full derivation of the kinetic equation. arXiv, 2104.11204v4, https://doi.org/10.48550/arXiv.2104.11204.

Dong, W., O. Bühler, and K. S. Smith, 2020: Frequency diffusion of waves by unsteady flows. *J. Fluid Mech.*, **905**, R3, https://doi.org/10.1017/jfm.2020.837.

——, ——, and ——, 2023: Stationary inertia–gravity wave frequency spectra generated by geostrophic flow refractions. *J. Phys. Oceanogr.*, **53**, 1311–1322, https://doi.org/10.1175/JPO-D-22-0153.1.

Eliassen, A., and E. Palm, 1961: On the transfer of energy in stationary mountain waves. *Geofys. Publ.*, **22**, 1–23.

Fouque, J.-P., J. Garnier, G. Papanicolaou, and K. Sølna, 2007: *Wave Propagation and Time Reversal in Randomly Layered Media*. Springer, 612 pp.

Frankignoul, C., and T. M. Joyce, 1979: On the internal wave variability during the internal wave experiment (IWEX). *J. Geophys. Res.*, **84**, 769–776, https://doi.org/10.1029/JC084iC02p00769.

Gargett, A. E., 1990: Do we really know how to scale the turbulent kinetic energy dissipation rate $\varepsilon$ due to breaking of oceanic internal waves? *J. Geophys. Res.*, **95**, 15 971–15 974, https://doi.org/10.1029/JC095iC09p15971.

Gershgorin, B., Y. V. Lvov, and S. Nazarenko, 2009: Canonical Hamiltonians for waves in inhomogeneous media. *J. Math. Phys.*, **50**, 013527, https://doi.org/10.1063/1.3054275.

Gregg, M. C., 1989: Scaling turbulent dissipation in the thermocline. *J. Geophys. Res.*, **94**, 9686–9698, https://doi.org/10.1029/JC094iC07p09686.

——, T. B. Sanford, and D. P. Winkel, 2003: Reduced mixing from the breaking of internal waves in equatorial waters. *Nature*, **422**, 513–515, https://doi.org/10.1038/nature01507.

Henyey, F. S., 1991: Scaling of internal wave model predictions for. *Dynamics of Oceanic Internal Gravity Waves: Proc. ʻAha Huliko'a Hawaiian Winter Workshop*, Honolulu, HI, University of Hawaiʻi at Mānoa, 233–236, https://www.soest.hawaii.edu/PubServices/1991pdfs/Henyey2.pdf.

——, J. Wright, and S. M. Flatté, 1986: Energy and action flow through the internal wave field. An eikonal approach. *J. Geophys. Res.*, **91**, 8487–8495, https://doi.org/10.1029/JC091iC07p08487.

Hibiya, T., N. Furuichi, and R. Robertson, 2012: Assessment of fine-scale parameterizations of turbulent dissipation rates near mixing hotspots in the deep ocean. *Geophys. Res. Lett.*, **39**, L24601, https://doi.org/10.1029/2012GL054068.

Holloway, G., 1980: Oceanic internal waves are not weak waves. *J. Phys. Oceanogr.*, **10**, 906–914, https://doi.org/10.1175/1520-0485(1980)010<0906:OIWANW>2.0.CO;2.

——, 1982: On interaction time scales of oceanic internal waves. *J. Phys. Oceanogr.*, **12**, 293–296, https://doi.org/10.1175/1520-0485(1982)012<0293:OITSOO>2.0.CO;2.

——, and M. C. Hendershott, 1977: Stochastic closure for nonlinear Rossby waves. *J. Fluid Mech.*, **82**, 747–765, https://doi.org/10.1017/S0022112077000962.

Ijichi, T., and T. Hibiya, 2015: Frequency-based correction of finescale parameterization of turbulent dissipation in the

Brought to you by MBL/WHOI Library | Unauthenticated | Downloaded 06/09/25 01:56 PM UTC

deep ocean. *J. Atmos. Oceanic Technol.*, **32**, 1526–1535, https://doi.org/10.1175/JTECH-D-15-0031.1.

——, and ——, 2017: Eikonal calculations for energy transfer in the deep-ocean internal wave field near mixing hotspots. *J. Phys. Oceanogr.*, **47**, 199–210, https://doi.org/10.1175/JPO-D-16-0093.1.

Jones, W. L., 1967: Propagation of internal gravity waves in fluids with shear flow and rotation. *J. Fluid Mech.*, **30**, 439–448, https://doi.org/10.1017/S0022112067001521.

——, 1969: Ray tracing for internal gravity waves. *J. Geophys. Res.*, **74**, 2028–2033, https://doi.org/10.1029/JB074i008p02028.

Kafiabad, H. A., M. A. C. Savva, and J. Vanneste, 2019: Diffusion of inertia-gravity waves by geostrophic turbulence. *J. Fluid Mech.*, **869**, R7, https://doi.org/10.1017/jfm.2019.300.

Kolmogorov, A. N., 1941: Local structure of turbulence in an incompressible fluid at very high Reynolds numbers. *Dokl. Akad. Nauk SSSR*, **30**, 299–303.

Kraichnan, R. H., 1959: The structure of isotropic turbulence at very high Reynolds numbers. *J. Fluid Mech.*, **5**, 497–543, https://doi.org/10.1017/S0022112059000362.

——, 1965: Lagrangian-history closure approximation for turbulence. *Phys. Fluids*, **8**, 575–598, https://doi.org/10.1063/1.1761271.

Lagendijk, A., B. van Tiggelen, and D. S. Wiersma, 2009: Fifty years of Anderson localization. *Phys. Today*, **62**, 24–29, https://doi.org/10.1063/1.3206091.

Leaman, K. D., and T. B. Sanford, 1975: Vertical energy propagation of inertial waves: A vector spectral analysis of velocity profiles. *J. Geophys. Res.*, **80**, 1975–1978, https://doi.org/10.1029/JC080i015p01975.

Lesieur, M., 1997: *Turbulence in Fluids*. Fluid Mechanics and Its Applications, Vol. 40, Kluwer Academic Publishers, 515 pp.

Lvov, Y. V., and E. G. Tabak, 2004: A Hamiltonian formulation for long internal waves. *Physica D*, **195**, 106–122, https://doi.org/10.1016/j.physd.2004.03.010.

——, and K. L. Polzin, 2024: Generalized transport characterizations for short oceanic internal waves in a sea of long waves. *J. Fluid Mech.*, **987**, A43, https://doi.org/10.1017/jfm.2024.337.

——, ——, E. G. Tabak, and N. Yokoyama, 2010: Oceanic internal-wave field: Theory of scale-invariant spectra. *J. Phys. Oceanogr.*, **40**, 2605–2623, https://doi.org/10.1175/2010JPO4132.1.

——, ——, and N. Yokoyama, 2012: Resonant and near-resonant internal wave interactions. *J. Phys. Oceanogr.*, **42**, 669–691, https://doi.org/10.1175/2011JPO4129.1.

MacKinnon, J. A., M. H. Alford, O. Sun, R. Pinkel, Z. Zhao, and J. Klymak, 2013: Parametric subharmonic instability of the internal tide at 29°N. *J. Phys. Oceanogr.*, **43**, 17–28, https://doi.org/10.1175/JPO-D-11-0108.1.

——, and Coauthors, 2017: Climate process team on internal wave–driven ocean mixing. *Bull. Amer. Meteor. Soc.*, **98**, 2429–2454, https://doi.org/10.1175/BAMS-D-16-0030.1.

McComas, C. H., III, 1975: Nonlinear interaction of internal gravity waves. Ph.D. thesis, The Johns Hopkins University, 24 pp., https://www.proquest.com/openview/f7d2bd7c6126ddd095b290abf9dcdc1e/1.pdf?pq-origsite=gscholar&cbl=18750&diss=y.

——, 1977: Equilibrium mechanisms within the oceanic internal wave field. *J. Phys. Oceanogr.*, **7**, 836–845, https://doi.org/10.1175/1520-0485(1977)007<0836:EMWTOI>2.0.CO;2.

——, and F. P. Bretherton, 1977: Resonant interaction of oceanic internal waves. *J. Geophys. Res.*, **82**, 1397–1412, https://doi.org/10.1029/JC082i009p01397.

——, and P. Müller, 1981a: Time scales of resonant interactions among oceanic internal waves. *J. Phys. Oceanogr.*, **11**, 139–147, https://doi.org/10.1175/1520-0485(1981)011<0139:TSORIA>2.0.CO;2.

——, and ——, 1981b: The dynamic balance of internal waves. *J. Phys. Oceanogr.*, **11**, 970–986, https://doi.org/10.1175/1520-0485(1981)011<0970:TDBOIW>2.0.CO;2.

McWilliams, J. C., 1976: Maps from the mid-ocean dynamics experiment: Part I. Geostrophic streamfunction. *J. Phys. Oceanogr.*, **6**, 810–827, https://doi.org/10.1175/1520-0485(1976)006<0810:MFTMOD>2.0.CO;2.

Meiss, J. D., N. Pomphrey, and K. M. Watson, 1979: Numerical analysis of weakly nonlinear wave turbulence. *Proc. Natl. Acad. Sci. USA*, **76**, 2109–2113, https://doi.org/10.1073/pnas.76.5.2109.

Müller, P., 1976: On the diffusion of momentum and mass by internal gravity waves. *J. Fluid Mech.*, **77**, 789–823, https://doi.org/10.1017/S0022112076002899.

——, and D. J. Olbers, 1975: On the dynamics of internal waves in the deep ocean. *J. Geophys. Res.*, **80**, 3848–3860, https://doi.org/10.1029/JC080i027p03848.

——, G. Holloway, F. Henyey, and N. Pomphrey, 1986: Nonlinear interactions among internal gravity waves. *Rev. Geophys.*, **24**, 493–536, https://doi.org/10.1029/RG024i003p00493.

Munk, W., 1981: Internal waves and small-scale processes. *Evolution of Physical Oceanography*, B. A. Warren and C. Wunsch, Eds., MIT Press, 264–291.

Nazarenko, S., 2011: *Wave Turbulence*. Springer, 279 pp.

——, A. C. Newell, and S. Galtier, 2001: Non-local MHD turbulence. *Physica D*, **152–153**, 646–652, https://doi.org/10.1016/S0167-2789(01)00197-X.

Ogura, Y., 1963: A consequence of the zero-fourth-cumulant approximation in the decay of isotropic turbulence. *J. Fluid Mech.*, **16**, 33–40, https://doi.org/10.1017/S0022112063000562.

Olbers, D. J., 1973: *On the Energy Balance of Small-Scale Internal Waves in the Deep-Sea*. Hamburger Geophysikalische Einzelschriften, Vol. 24, G. M. L. Wittenborn Sohnes, 91 pp.

——, F. Pollmann, and C. Eden, 2020: On PSI interactions in internal gravity wave fields and the decay of baroclinic tides. *J. Phys. Oceanogr.*, **50**, 751–771, https://doi.org/10.1175/JPO-D-19-0224.1.

Orzag, S. A., 1973: Statistical theory of turbulence. *Fluid Dynamics*, R. Balian and J. L. Peube, Eds., Gordon and Breach, 237–374.

Polzin, K., 2004a: A heuristic description of internal wave dynamics. *J. Phys. Oceanogr.*, **34**, 214–230, https://doi.org/10.1175/1520-0485(2004)034<0214:AHDOIW>2.0.CO;2.

——, 2004b: Idealized solutions for the energy balance of the finescale internal wave field. *J. Phys. Oceanogr.*, **34**, 231–246, https://doi.org/10.1175/1520-0485(2004)034<0231:ISFTEB>2.0.CO;2.

——, 2008: Mesoscale eddy–internal wave coupling. Part I: Symmetry, wave capture, and results from the Mid-Ocean Dynamics Experiment. *J. Phys. Oceanogr.*, **38**, 2556–2574, https://doi.org/10.1175/2008JPO3666.1.

——, 2009: An abyssal recipe. *Ocean Model.*, **30**, 298–309, https://doi.org/10.1016/j.ocemod.2009.07.006.

——, 2010: Mesoscale eddy–internal wave coupling. Part II: Energetics and results from PolyMode. *J. Phys. Oceanogr.*, **40**, 789–801, https://doi.org/10.1175/2009JPO4039.1.

——, and Y. S. Lvov, 2011: Toward regional characterizations of the oceanic internal wavefield. *Rev. Geophys.*, **49**, RG4003, https://doi.org/10.1029/2010RG000329.

Brought to you by MBL/WHOI Library | Unauthenticated | Downloaded 06/09/25 01:56 PM UTC

——, and ——, 2017: An oceanic ultra-violet catastrophe, wave-particle duality and a strongly nonlinear concept for geophysical turbulence. *Fluids*, **2**, 36, https://doi.org/10.3390/fluids2030036.

——, J. M. Toole, and R. W. Schmitt, 1995: Finescale parameterizations of turbulent dissipation. *J. Phys. Oceanogr.*, **25**, 306–328, https://doi.org/10.1175/1520-0485(1995)025<0306:FPOTD>2.0.CO;2.

——, A. C. Naveira Garabato, T. N. Huussen, B. M. Sloyan, and S. N. Waterman, 2014: Finescale parameterizations of turbulent dissipation. *J. Geophys. Res. Oceans*, **119**, 1383–1419, https://doi.org/10.1002/2013JC008979.

Rhines, P. B., and W. R. Young, 1982: Homogenization of potential vorticity in planetary gyres. *J. Fluid Mech.*, **122**, 347–367, https://doi.org/10.1017/S0022112082002250.

Ruddick, B. R., and T. M. Joyce, 1979: Observations of interaction between the internal wavefield and low-frequency flows in the North Atlantic. *J. Phys. Oceanogr.*, **9**, 498–517, https://doi.org/10.1175/1520-0485(1979)009<0498:OOIBTI>2.0.CO;2.

Sanford, T. B., 1975: Observations of the vertical structure of internal waves. *J. Geophys. Res.*, **80**, 3861–3871, https://doi.org/10.1029/JC080i027p03861.

Savva, M. A. C., and J. Vanneste, 2018: Scattering of internal tides by barotropic quasigeostrophic flows. *J. Fluid Mech.*, **856**, 504–530, https://doi.org/10.1017/jfm.2018.694.

——, H. A. Kafiabad, and J. Vanneste, 2021: Inertia-gravity-wave scattering by three-dimensional geostrophic turbulence. *J. Fluid Mech.*, **916**, A6, https://doi.org/10.1017/jfm.2021.205.

Sheng, P., and B. van Tigglen, 2007: *Introduction to Wave Scattering, Localization and Mesoscopic Phenomena.* Taylor & Francis, 333 pp.

Sun, H., and E. Kunze, 1999a: Internal wave–wave interactions. Part I: The role of internal wave vertical divergence. *J. Phys. Oceanogr.*, **29**, 2886–2904, https://doi.org/10.1175/1520-0485(1999)029<2886:IWWIPI>2.0.CO;2.

——, and ——, 1999b: Internal wave–wave interactions. Part II: Spectral energy transfer and turbulence production. *J. Phys. Oceanogr.*, **29**, 2905–2919, https://doi.org/10.1175/1520-0485(1999)029<2905:IWWIPI>2.0.CO;2.

Taylor, G. I., 1922: Diffusion by continuous movements. *Proc. London Math. Soc.*, **s2–20**, 196–212, https://doi.org/10.1112/plms/s2-20.1.196.

Thurnherr, A. M., L. Clément, L. St. Laurent, R. Ferrari, and T. Ijichi, 2020: Transformation and upwelling of bottom water in fracture zone valleys. *J. Phys. Oceanogr.*, **50**, 715–726, https://doi.org/10.1175/JPO-D-19-0021.1.

Treguier, A. M., I. M. Held, and V. D. Larichev, 1997: Parameterization of quasigeostrophic eddies in primitive equation ocean models. *J. Phys. Oceanogr.*, **27**, 567–580, https://doi.org/10.1175/1520-0485(1997)027<0567:POQEIP>2.0.CO;2.

Watson, K. M., 1985: Interaction between internal waves and mesoscale flow. *J. Phys. Oceanogr.*, **15**, 1296–1311, https://doi.org/10.1175/1520-0485(1985)015<1296:IBIWAM>2.0.CO;2.

Whalen, C. B., 2021: Best practices for comparing ocean turbulence measurements across spatiotemporal scales. *J. Atmos. Oceanic Technol.*, **38**, 837–841, https://doi.org/10.1175/JTECH-D-20-0175.1.

Wijesekera, H., L. Padman, T. Dillon, M. Levine, C. Paulson, and R. Pinkel, 1993: The application of internal-wave dissipation models to a region of strong mixing. *J. Phys. Oceanogr.*, **23**, 269–286, https://doi.org/10.1175/1520-0485(1993)023<0269:TAOIWD>2.0.CO;2.

Yang, L., R. Barkan, K. Srinivasan, J. C. McWilliams, C. J. Shakespeare, and A. H. Gibson, 2023: Oceanic eddies induce a rapid formation of an internal wave continuum. *Commun. Earth Environ.*, **4**, 484, https://doi.org/10.1038/s43247-023-01137-1.

Zakharov, V. E., V. S. Lvov, and G. Falkovich, 1992: *Kolmogorov Spectra of Turbulence*. Springer-Verlag, 264 pp.

Zhao, Z., M. H. Alford, J. B. Girton, L. Rainville, and H. L. Simmons, 2016: Global observations of open-ocean mode-1 $M_2$ internal tides. *J. Phys. Oceanogr.*, **46**, 1657–1684, https://doi.org/10.1175/JPO-D-15-0105.1.

Brought to you by MBL/WHOI Library | Unauthenticated | Downloaded 06/09/25 01:56 PM UTC